Title
Insights into the sea-level history of the South Shetland Islands from ground penetrating radar on Livingston Island, Antarctica

Journal
Quaternary Science Reviews, 359

ISSN
0277-3791

Authors
Gernant, Cameron
Simms, Alexander R
DeWitt, Regina
et al.

Publication Date
2025-07-01

DOI
10.1016/j.quascirev.2025.109363

Insights into the Sea-Level History of the South Shetland Islands from Ground Penetrating Radar on Livingston Island, Antarctica

Cameron Gernant[1], Alexander R. Simms[1], Regina DeWitt[2], Brittany Theilen[1], Christopher N. Garcia[2], and Michael Goebel[3]

[1]Department of Earth Science, University of California Santa Barbara, Santa Barbara, CA 93106

[2]Department of Physics, East Carolina University, Greenville, NC 27858

[3]Institute of Marine Sciences, University of California Santa Cruz, Santa Cruz, CA 95064

Abstract

Sea-level changes in polar environments are important for understanding the timing and magnitude of past ice-sheet changes. Most of the few records of such past sea-level changes in Antarctica are those derived from raised beach ridges. Many studies using raised beach ridges to reconstruct past sea levels across Antarctica commonly assume that they only record falling sea levels. However, their internal architecture may contain a record of other oscillations in relative sea-level (RSL) change. In this study, we examine the internal architecture of a well-developed set of raised beach ridges on Livingston Island of the Antarctic Peninsula using 10+ km of ground penetrating radar (GPR). Recalibrated published radiocarbon ages are used in combination with new optically stimulated luminescence (OSL) ages to compare beach morphology and stratigraphy to the glacial history of the region. Within this flight of raised beach ridges, evidence was found for both regressive and transgressive depositional patterns marked by progradational seaward dipping facies deposited during periods of RSL fall followed by erosion and deposition of landward dipping overwash and aggrading beds during interpreted periods of RSL rise. This succession is routinely located over a notch in the bedrock interpreted to represent a wave-cut feature. The ages of raised beach ridges underlain by wave-cut notches and composed of landward-dipping strata correlate with known Holocene ice advances at <500, ~2000, and ~5000 cal yrs BP. We propose that these transgressive phases are the result of glacial-isostatic adjustment (GIA). This GIA hypothesis further

supports recent assertions of a much more dynamic RSL history for Antarctic coastlines, which may contaminate the Last Glacial Maximum RSL signal across Antarctica.

1. Introduction

The Antarctic Peninsula (AP) (Fig. 1) contains enough meltwater equivalent ice to raise global sea-levels by 2.4 m (Pritchard and Vaughan, 2007). Understanding how ice along the AP will contribute to future sea-level rise is important for coastal hazard mitigation (IPCC, 2019; Pörtner et al., 2022). One way to better understand how this region's ice sheet might change in the future is by studying how it responded to past climate changes. Such studies include not only mapping out the ice sheet's past distribution, which can constrain the aerial distribution of that ice, but also reconstructing past sea levels, which in combination with glacial-isostatic adjustment (GIA) model predictions can help constrain its past ice thicknesses. Despite their importance in the latter of these two constraints, RSL reconstructions for Antarctica are more poorly constrained than the more northern continents.

Raised beach ridges, along with isolation basins, are the most common means of reconstructing past RSLs across Antarctica (Hall 2010; Bentley et al., 2005a; Simms, 2023). Not only do they preserve a record of past sea-level elevations, but also environmental conditions (e.g. Simkins et al., 2015; Lindhorst and Schutter, 2014; Theilen et al., 2023). These past environmental conditions are often recorded in their stratigraphic architecture (e.g. Lindhorst and Schutter, 2014; Theilen et al., 2023). On mixed sand-gravel beaches ground penetrating radar (GPR) provides an excellent method for documenting that stratigraphic architecture (Lindhorst and Schutter, 2014; Nielsen et al., 2017).

Previous studies have hypothesized periods of minor transgression during the overall fall in RSLs following significant ice loss since the Last Glacial Maximum (LGM; John and Sugden, 1971; Curl, 1980; Bentley et al., 2005b; Hall, 2010), but evidence for those minor transgressions is sparse (Bentley et al., 2005b; Hall, 2009; Watcham et al., 2011). Such evidence may be found buried beneath the subsurface in the stratigraphic architecture of the raised beach ridges of the South Shetland Islands (SSI). The purpose of this study is to use GPR to characterize the stratigraphic architecture of the South Beaches on Byers Peninsula of Livingston Island of the SSI (Fig. 1). In addition, we use optically stimulated luminescence (OSL) to add to the existing chronology for these raised beach ridges.

2. Background

2.1. Geologic Setting

The SSI chain is a roughly 500 km long island arc situated in maritime sub-Antarctica. Together the two largest islands, Livingston Island and King George Island (KGI), are spread over an area 230 km long but only 35 km wide (Fig. 1) (Adie, 1977; Smellie et al., 1984). They separate the Bransfield Basin to the south from the Drake Passage to the north (Gracia et al., 1997). The islands are surrounded by a shallow submarine platform extending 40 to 60 km north of the islands (Fretwell et al., 2010; Simms et al., 2011b). To the south, the continental shelf is narrower with widths less than 5 km in some locations (Lawver et al., 1996; Simms et al., 2011).

Although subduction has ceased over the rest of the northern AP, subduction continues along an ~400 km section beneath the SSI (Robertson et al., 2003; Jin et al., 2009). The subduction zone is seismically active with as many as 150 magnitude 2-5 local earthquakes at depths up to 65 km, with most less than 30 km, detected between 1997-1999 (Robertson et al., 2003). However, few earthquakes greater than 5 have been observed across the islands (Robertson et al., 2003). As a result of this subduction, the SSI are likely experiencing tectonic uplift, potentially co-seismic in nature. The long-term tectonic uplift rates for the SSI have been estimated at between 0.39 and 0.48 m/ka using undated but assumed Marine Isotope Stages (MIS) 5e, 7, and 9 marine platforms as proxies for uplift (Pallas et al., 1997; Watcham et al., 2011). If uplift were constant through the Holocene, the range in long-term tectonic uplift rates of between 0.39 and 0.48 m/ka yields 3.2 to 3.8 m of the 15.5 m of total uplift over the last ~8000 years on Fildes Peninsula of KGI suggesting GIA dominates the RSL curve (Pallas et al., 1997; Watcham et al., 2011).

2.2. Glacial History

At some point in the past, most likely during the LGM, the SSI were covered by a grounded ice sheet that extended all the way to the shelf edge, along its southern and northern shelves (John and Sugden, 1971; Hall et al., 2009; Simms et al., 2011b; O'Cofaigh et al., 2014). At this time, an ice shelf likely extended across the Bransfield Basin connecting the SSI to the AP (Simms et al., 2011b; John and Sugden, 1971). Deglaciation of Byers Peninsula, the largest ice-free area on Livingston Island, progressed from west to east initiating at ~8,000 cal yrs BP (Toro et al., 2013; Oliva et al., 2016; Ruiz-Fernandez and Oliva, 2016). By 6,000 cal yrs BP glaciers on the AP across the Bransfield Basin were similar to, or smaller than present-day ice extent (Charman et al., 2018). Evidence for multiple smaller advances and ice retreats through the Holocene are found across the SSI (Hall, 2009; Palacios et al., 2020; Simms et al., 2021; Heredia Barion et al., 2023a,b). Although the timing of these advances is still being refined, they appear to have been around 4,000 to 5,000 cal yrs BP, 1800 cal yrs BP and within the last 700 years (Heredia Barion et al., 2023a,b). Intervening periods of ice-free conditions with glacial ice landward of present ice margins is found in the form of re-exposed moss banks (Yu et al., 2016; Charman et al., 2018).

2.3. Glacio-Isostatic Adjustment (GIA) and Sea Level

Despite global rising eustatic sea levels through the Holocene, RSL fell in near-field regions, which experienced ice-mass loss and thus post-glacial rebound (Bentley et al., 2005a; Whitehouse, 2018; Palacios et al., 2020). Fretwell et al. (2010) mapped isobars of equivalent patterns of raised beach ridges throughout the SSI interpreted to represent differential isostatic uplift experienced throughout the island chain. This map supports prior assertions of the ice cap being centered along the axis of the SSI chain (John and Sugden, 1971; Curl, 1980) during the local LGM (Simms et al., 2011b).

The solid earth beneath the SSI and the AP appears to be more responsive to ice mass changes than other places across the globe (Thomas et al., 2011; Simms et al., 2012; Whitehouse et al., 2012; Nield et al., 2014; Simms et al., 2018). After the Larsen-B ice sheet breakup, which buttressed valley glaciers from unimpeded flow into the ocean, GPS recorded uplift rates at Palmer Station on the western AP ~300 km to the south of the SSI increased from 0.08 ± 1.87 mm/a to 8.75 ± 0.64 mm/a (Thomas et al., 2011). Nield et al. (2014) showed that at least some of that uplift had to be viscoelastic in nature. This response suggests the earth beneath the AP, including the SSI, may be sensitive to Holocene ice-mass fluctuations other than just post-LGM ice-mass loss (Nield et al., 2014; Simms et al., 2012; 2018; Zurbuchen and Simms, 2019).

2.4. Raised Beaches

Raised beaches are the most widely used geomorphic feature for reconstructing paleo-sea-level in polar environments (Baroni and Hall, 2004; Hall and Denton, 1999; Hall and Perry, 2004; Hall, 2007; Hall, 2010; Simms et al., 2011a; Tamura, 2012; Zurbuchen and Simms, 2019; Simms, 2023). Sea-level index points from beach ridge crests are used with the assumption that beach ridges form at a known elevation above sea level during storms or fair-weather wave conditions. However, beach-ridge elevation is a function of not only mean sea level, but also wave energy, storm energy, tidal range, grain size and shape, and sediment availability (Taylor and Stone, 1996; Lindhorst and Schutter, 2014; Scheffers et al., 2012), as well as bathymetric profile and underlying onshore bedrock topography. Thus, their indicative meaning varies regionally but is generally around +2 m (Otvos, 2000; Hall, 2010; Lindhorst and Schutter, 2014).

RSL curves derived from these features in Antarctica including the SSI, primarily record sea-level fall caused from glacio-isostatic uplift (John and Sugden, 1971; Bentley et al., 2005a; Watcham et al., 2011; Hall, 2010). Recently, studies have focused on using the internal stratigraphy and geometry of raised beaches to refine their use in sea-level and other paleoenvironmental reconstructions (Nielsen and Clemmensen, 2009; Lindhorst and Schutter, 2014; Costas et al., 2016; Nielsen et al., 2017).

Raised beaches and isolation basins in Antarctica have been dated with radiocarbon (^{14}C) (Hall and Perry, 2004; Watcham et al., 2011; Zurbuchen and Simms, 2019), OSL (Simms et al., 2011; Simkins et al., 2013; Hong et al., 2021; Theilen et al., 2023), and more recently cosmogenic nuclides (Yıldırım et al., 2024). However, using ^{14}C to date in Antarctica is difficult due to uncertainties in the ^{14}C reservoir and the dearth of organic material to date. Suggested ^{14}C reservoir corrections range from 500 to 1400 years (Bentley et al, 2005b; Hall et al., 2010b; Divola et al., 2024). In addition to the uncertainties of the ^{14}C reservoir, the sparse organic material found in Antarctica results in the use of reworked bones and organic material on the beach surface, typically yielding only minimum or maximum ages for the beaches (Hansom, 1979; Bentley et al., 2005a; Hall, 2010). Furthermore, some beach ridges are composite features from pre-LGM times (e.g. Gardner et al., 2006), making their cores older than the usefulness of radiocarbon dating. Optically stimulated luminescence provides promise, but its application to the beaches of Antarctica has been received with mixed results (e.g. Simkins et al., 2016; Theilen et al., 2023), most notably due to the generally dim nature of the quartz in many Antarctic materials.

2.5. Livingston Island Field Site

2.5.1. Location and Beach Characteristics

Livingston Island is located approximately 160 km north of the AP in the northeast-southwest trending Sub-Antarctic SSI. With a total area of 798 km^2, the island is the second largest in the SSI after KGI (1,150 km^2) located ~80 km to the northeast (Fig. 1). Byers Peninsula (62°34'35"-62°40'35"S, 60°54'14"-61°13'07"W) on the western end of Livingston Island is the largest ice-free region in the SSI (60 km^2), followed by Fildes Peninsula on KGI (29 km^2). Rotch Dome Glacier covers the majority of the island including the eastern end of Byers Peninsula. It reaches a maximum elevation of 360 m (Palacios et al., 2020).

The bedrock on Byers Peninsula is mainly composed of weak beds of marine shales and sandstone of the Carboniferous Miers Bluff Series interbedded with friable dyke-intruded basaltic agglomerates and augite-andesites of the Miocene Younger Volcanic Group (Adie, 1964; Barton, 1965; Hobbs, 1968). The oldest rocks on Livingston Island are the False Bay Schists, which are Precambrian or early Paleozoic in age (Hobbs, 1968).

The geomorphology of Byers Peninsula is comprised of a set of no fewer than four terraces, suggested to be of marine origin because of their similarity in shape to the modern shoreline, their near uniform elevations, and their gently seaward dipping orientations (John and Sugden, 1971; Curl, 1980). The central platform at 85-100 m gently slopes from the center outward in all directions towards the sea. The 28-50 m platform on the periphery of the central platform parallels the modern coastline more closely than the central platform. This platform is less dissected by meltwater channels than the central platform and retains several remnant stacks. It dips gently seaward at 0.5 to 1°, ending in a steep slope with gradients up to 30° above the 11-17 m platform. All major platforms above the 11-17 m platform are believed to have formed prior to the LGM (Sugden and John, 1973; Simms et al., 2024). The 11-17 m platform is less altered than the two higher platforms and retains paleo sea stacks 2-4 m high (Hansom, 1983). It dips seaward around 1 to 2° and is dissected by even fewer gullies than the 28-50 m marine platform. The gullies that dissect the 11-17 m platform are linked to streams that dissect the overlying raised beach ridges (Fig. 2) and source sediment to alluvial fans onshore and the modern beach. The formation age of the ~3-8 m platform underlying the raised beaches is less clear, because these platforms commonly rest within glacial troughs suggesting they formed after earlier glaciations. Striations on the 3-8 m platform are interpreted by some as related to a pre-local LGM glaciation (John and Sugden, 1971) and by others as abrasion from debris-rich ice (Hansom, 1983), suggesting they may post-date the local LGM or one of the later phases of Holocene glacial advance.

Holocene raised beach ridges across the SSI cluster into three groups: 4 to 6 m, 8 to 12 m, and 15 to 20 m in elevation and overlie the 11 to 17 and 3 to 8 m platform (John and Sugden, 1971; Barsch and Mäusbacher, 1986; Simms et al., 2012). The same groups are found on Byers Peninsula but at lower elevations than similar aged raised beach ridges located closer to the center of ice loading (Fretwell et al., 2010) (Figs. 2 and 3). Previous work on Livingston Island was only successful in dating raised beach ridges lower than ~11 m. The 4-6 m elevation beach ridges of the South Beaches date to 400-700 cal yrs BP (Curl, 1980; Hall, 2010; Hall, 2003; Hall and Perry, 2004), the 8-12 m raised beach ridges date to 1800-2600 cal yrs BP (Hall and Perry, 2004; Hansom, 1979; Hall, 2010). On other islands the 15-20 m raised beach ridges date to 6000-7000 cal yrs BP (Hall, 2010). Hall (2010) extrapolates the RSL curve to the marine limit of 18-21 m on Byers Peninsula, which yields an age of 7500 cal yrs BP, similar to the age of the marine limit on nearby KGI (Watcham et al., 2011), but notes that this more than likely relates to a transgression. Regional evidence (Sugden and John, 1973; Mäusbacher et al., 1989; Toro et al., 2013; Oliva et al., 2016) suggests that ice recession began earlier between ~8300 to ~9500 cal yrs BP.

This study focuses on an area located on the South Beaches of Byers Peninsula (Fig. 2). The beaches studied, range in width from 500-1100 m and extend 9.7 km in length from Clark Nunatak in the east to Vietor Rock in the west with a tombolo west of Cerro Negro (Fig. 2) located near the center (Hobbs, 1968) (Fig. 4). A similar set of raised beaches, Robbery Beaches, lie on the north side of Byers Peninsula but are thinner with a maximum width of 100 m (Fig. 1). This difference is likely due to differences between the submarine profile of the northern and southern sides of Byers Peninsula. The northern Byers Peninsula shelf has a slope of 124 m/1.6 km (slope=0.077) while the southern Byers Peninsula shelf has a slope of 18 m/1.6 km (slope=0.0112) (Curl, 1980). This submarine profile further serves to partially protect the south facing beaches from storm waves as they break farther offshore thus limiting erosion. The mixed sand-gravel and pebble clasts forming the beaches (Fig. 3) are derived from the Younger Volcanic Group (Hobbs, 1968). They unconformably lie on the lower marine terraces with bedrock supported beach deposit depths up to 2 m where measured (John and Sugden, 1971) in the surveyed area. Tonalite cobbles are found on beach ridge crests and are thought to have traveled via longshore currents from Barnard Point, Livingston Island (Hobbs, 1968). Non-local ice-rafted debris (IRD) from the AP is also found on several of the raised beach ridges whose higher abundance on some raised beach ridges are interpreted by Hall and Perry (2004) to represent cooler periods when debris-laden icebergs would travel farther distances.

2.5.2. Climatic Setting

At an elevation of 80 m on Livingston Island the average annual temperature is -2.8 °C and the average annual precipitation is 650 mm (John and Sugden, 1971; Bañón et al., 2013; De Pablo et al., 2014). At an elevation of 70 m on Byers Peninsula, winds are predominantly from the west to northeast passing through north, with an average speed of 26 km/hr. Frequent storms with wind gusts exceeding 100 km/hr (max speed 139 km/hr) were recorded between 2001 and 2003 C.E. Calm periods represent just 1.4 % of the record (Bañón et al., 2013). The incident wind direction aids in creating larger storm waves on the western and northerly coasts where fetch is effectively limitless across the South Pacific Ocean (Hobbs, 1968; John and Sugden, 1971; Palacios et al., 2020). The southern coast is sheltered from these winds and storm waves to a higher degree, and fetch is limited to around 160 km – the width of the Bransfield Strait. Summer waves in the Bransfield Strait have wind wave periods of 1.2 s with a mean height of 0.5 m. The wind waves in the nearby Scotia Sea have a mean period of 3 to 5 s and a mean height of 2 m. The swell waves in the Bransfield Strait have a mean period of 3 s and a mean height of 1 m while in the Scotia Sea they are 7 to 8 s and 3 m, respectively (Hansom, 1983). Sea ice rarely extends to the northwest of the SSI but where encountered, can persist for up to 200 days per year in the southeastern and southern coasts and embayments of the SSI. These locations are also protected by fast ice for 6-8 months per year (Curl, 1980).

3. Methods

3.1. GNSS

Global positioning system (GPS) surveys of the beaches were conducted using a Trimble NetR9 with a Trimble Zephyr Geodetic 2 RoHS antenna as a base station and Trimble TSC2 R7 with a Trimble Zephyr Geodetic antenna for a Rover GPS unit. Roving Post Processing Kinematic (PPK) data was processed using Trimble Business Center (TBC). Coordinates are based on Datum Transformation ITRF2014, projection UTM Zone 20 South, and GEOID Model EGM96. Local base station data was incomplete resulting in large horizontal and vertical errors. Upon failure of the base station (G412) to collect adequate data during portions of the field campaign, GPS was processed using a continuous base station on Livingston Island ~35 km to the east of the field site (BEJ2 -62° 39' 46.88939", -60° 23' 9.42703") operated by researchers from the University of Cádiz, Spain. The Spanish, BEJ2 survey utilized a Trimble R7 GNSS Base Station with a Trimble Zephyr Geodetic 2 Dome. The Canadian Geodetic Survey (CGS) Precise Point Positioning (PPP) tool was used to process the base station coordinates. Horizontal and vertical precision averaged 1.5 ± 1.4 cm and 2.3 ± 1.9 cm across all data points and days surveyed.

3.2. Ground Penetrating Radar (GPR)

Ground penetrating radar surveys were conducted using a Sensors and Software Inc. pulseEKKO PRO system with 200 MHz antennas and a step size of 0.5 m. Profiles were taken normal to and along shore in order to reconstruct the architecture of the raised beaches (Fig. 2). The setup allowed a vertical resolution of 0.10 m. Surveys were processed using EkkoView Deluxe software from Sensors and Software Inc. The data processing included standard dewow processing, a bandpass filter, and automatic gain control. The data was migrated by converting two-way travel time (TWT) to depth using the average radar velocity (0.101 m/ns) derived from a common midpoint (CMP) survey collected in the field. Finally, the radar profiles were topographically corrected to show true geometric relationships in the subsurface using post-processed synchronously collected GPS data. Radar reflection geometry was traced and examined to differentiate and classify radar facies and surfaces. Radar facies and surfaces were identified with criteria outlined by Neal (2004). Radar facies were identified by shape, dip, reflection configuration, and continuity (Fig. 4). Radar surfaces were classified by their upper and lower boundaries as observed from reflection terminations in profile (Fig. 5).

3.3. Tide Gauge

A Valeport 740 Portable Water Level Recorder was deployed over the first three days of the field campaign before being entangled by kelp at 62° 39’45.7759” S, 61°0’42.8248” W. Mean tide level (MTL) was measured by averaging the mean high water and mean low water marks from the three days of data. The Livingston tide data was extended using the estimated 20-year National Tidal Datum Epoch (NTDE) for nearby Palmer Station following the NOAA Computational Techniques for Tidal Datums Handbook standard method for mixed tides (Evans et al., 2003). The corrected MTL for Livingston Island is +0.790 m relative to mean tide level (Theilen, 2020). This elevation offset was used to adjust the Trimble GPS elevations to local mean sea level (MSL) (Theilen, 2020).

3.4. Optically Stimulated Luminescence (OSL) Dating

Samples of both cobbles and sand were collected for OSL dating. As most of the cobbles composing the beaches were fine-grained, presumably siltstones or volcanics, we focused our cobble sampling on out-of-place granitic or andesitic rocks, presumably ice-rafted debris (e.g. Hall and Perry, 2004). In addition, we dug ~50 cm deep trenches into the strandplains to observe their sedimentary structures and collect sand samples for OSL dating from the walls of the trench. Samples were collected by use of an opaque tarp draped over the area during sampling. Approximately 1 kg of sediment was collected from the surrounding beach materials for use in determining the natural dose rate.

Sample preparation and OSL dating methods followed Simkins et al. (2016). For cobbles, the outer 1 mm surface of the lower light-shielded part was separated following Simms et al. (2011a), who demonstrated that this layer was reset completely after one hour of daylight exposure. The target slices were crushed by hand using a mortar and pestle in order to avoid pressures that could erase the luminescence signal (Bateman et al., 2012). The subsequent treatment for cobble grains was the same as for sediment samples and followed standard procedures. The material was sieved for grain sizes 63-250 µm; in cases with exceptionally small amounts of sample material, grains up to 500 µm were used. The grains were then treated with 10% HCl and 27% H_2O_2 to remove carbonate and organic material contaminates. The remaining sediment from sand and cobble samples were density separated with lithium polytungstate liquid (LST) at specific gravities of 2.75, 2.62, 2.58, and 2.54 to isolate quartz, potassium and sodium feldspars, heavy, and light grains. Feldspar grains were etched using 10 % hydrofluoric acid for 15 min. For some samples it was not possible to separate sodium and potassium feldspars due to lack of material, and these samples were treated as “mixed” feldspars.

Measurements were conducted using a Risø TL/OSL-DA-20 reader, Risø National Laboratory, with a bialkali PM tube (Thorn EMI 9635QB). The built-in $^{90}Sr/^{90}Y$ beta source gives a dose rate of ~100 mGy/s. The exact dose rate value was calculated for the specific day on which each sample was measured. Feldspars were stimulated with an IR LED array at 870 nm with 121 mW/cm^2 (90%) power at the sample and a blue or yellow filter combination for detection. The heating rate used was 5 °C/s. The measurement procedure for feldspar was based on the single aliquot regenerative-dose (SAR) procedure described by Murray and Wintle (2000) and Wintle and Murray (2006). The procedure was modified such that the same temperature and 60 s duration was used for cutheat and preheat steps (compare Blair et al., 2007). The preheat temperatures were determined for each sample with plateau and dose recovery tests. The equivalent dose D_e was determined with the central age model (Galbraith et al., 1999).

Calculation of the dose rate followed the procedure described in detail by Simms et al. (2011a). For cobbles, the top, light-exposed portions were crushed for dose rate estimates. Concentrations of natural uranium, ^{232}Th and potassium were measured with high resolution gamma spectrometry for crushed rocks, surrounding material, and sediments. All samples were in radioactive equilibrium. Water content for rocks was assumed to be 0. The water content for the surrounding materials and sediment samples was measured and has an uncertainty of 3%. Alpha, Beta, and gamma dose rates were calculated using the conversion factors published by Guérin et al. (2011). The internal K-concentrations in the feldspar samples (for single grains as well as average values) were measured with EPMA at UCSB. To calculate the resulting internal dose rates, the grain sizes of the feldspars in the rock samples were measured. For gamma dose rates from the rock samples themselves, correction factors were calculated to allow for the size of the cobbles, that is smaller than the range of gamma radiation. The cosmic dose rate, was calculated as described by Barbouti and Rastin (1983), Prescott and Stephan (1982), and Prescott and Hutton (1994). The effective thickness was assumed to be half the burial depth for sediments or the thickness of the rock for cobbles. The uncertainty was 5%. Feldspar ages were fading corrected as described by Auclair et al. (2003) and Wallinga et al. (2007) for the linear and non-linear dose ranges, respectively. All raw OSL ages reported in the tables are given as ka while when compared to calibrated radiocarbon ages in the text, they have been adjusted to cal yrs BP by subtracting 70 years (2020-1950).

3.5. Radiocarbon Age Dating

The single new and existing radiocarbon ages collected from the beaches of the SSI were recalibrated using the marine curve of Calib 8.2 (Reimer et al., 2004; Heaton et al., 2020). For that calibration, we used a local ΔR of 443 ± 135 years obtained from historically harvested whale bones across the Antarctic Peninsula by Divola et al. (2024). We added to that one new age collected from a whale bone obtained from one of the beaches at Cape Sherriff on Livingston Island. The radiocarbon age determination was run at the UCI W. M. Keck Carbon Cycle Accelerator Mass Spectrometry (KCCAMS) Facility at the University of California Irvine.

3.6. Indicative Meaning of the Beach Ridges

Several methods have been suggested for determining the indicative meaning of beach ridges. The elevation of these features relative to MSL is known to be influenced by wave and storm energy, tidal range, sediment grain size and supply, and nearshore bathymetry (Otvos, 2000; Scheffers et al., 2012; Lindhorst and Schutter, 2014). Accurately quantifying the specific paleo-MSL associated with each raised beach ridge is therefore challenging and carries inherent uncertainty.

For this study we followed the approach suggested by Fretwell et al. (2010) for the SSI, in which the modern beach was used as an analogue for interpreting the RSL significance of the higher beach ridges. As such, we subtracted the elevation of the modern beach (beach 1; 1.65 ± 0.20 m above mean sea level (amsl)) from the average crest elevations of the higher beach ridges to arrive at a paleo RSL estimate (Fig. 12).

We acknowledge that storm conditions vary, and that grain size differs between the modern beach and others (Fig. 9), which impacts beach morphology (Lindhorst and Schutter, 2014). However, the fundamental mechanism for preserving these features relies on their removal from the active beach, primarily through subsequent progradation of younger deposits and RSL fall. The observation that major raised beach levels show general elevation consistency across the SSI, despite variations in grain size and shore orientation and exposure (Fretwell et al., 2010; Lindhorst and Schutter, 2014), suggests a dominant regional control rather than purely local wave energy heterogeneity. Therefore, using the modern beach elevation at our specific study site as an analogue provides a reasonable estimate of the typical relationship between MSL and preserved beach ridge elevation under the local environmental conditions.

4. Results

4.1. Elevations

GPS surveys were collected along the crest of beach ridges 1 (modern beach), 2, 4, 5, and 9 (Figs. 2 and 6). Beach 1 is the modern beach where an 800 m survey along the crest has an average elevation of 1.65 ± 0.20 m amsl (Fig. 6). Above beach 1 lies a series of elevated beach ridges. Some of these raised beach ridges stand anomalously high compared to the seaward strandplains and other minor raised beaches (Figs. 2 and 3). These are referred to here as stranded beach ridges. Beach ridge 2 is the lowest of the stranded beach ridges identified on Byers Peninsula and has an average elevation of 4.29 ± 0.78 m amsl along two ~470 m surveys of its crest (Fig. 6). Beach ridge 2 is dissected by streams oriented normal to the coast fed by runoff from higher elevation platforms (Fig. 2). Beach ridge 2 is 3 m and 1.6 m higher than the surrounding strandplains to its seaward and landward sides, respectively (Figs. 7 and 8). Beach ridge 3 is a poorly formed beach ridge on the seaward flank of beach ridge 4 and its 3.85 ± 0.14 m amsl elevation was measured using 15 GPS points collected during sample collection. Beach ridge 4 is the second full-formed stranded beach ridge with an average elevation of 8.06 ± 1.03 m amsl (Fig. 6) along a cumulative 930 m transect measured along its crest and is in places amalgamated with beach ridge 5. The crest of beach ridge 4 is 4.6 m higher than the seaward strandplain and 0.2 m higher than the strandplain landward of beach ridge 5 (Figs. 7 and 8). Beach ridge 5 is the third stranded beach ridge and has an average elevation of 9.54 ± 0.70 m amsl along a 1400 m GPS survey of its crest (Fig. 6). Beach ridge 5 has a prominence of 5.9 m above the strandplain seaward of beach ridge 4 and 0.78 m higher than its landward strandplain (Figs. 7 and 8).

Beach ridges 6, 7, and 8 are weakly developed beach ridges within the strandplain landward of stranded beach ridges 4 and 5 and are only a few 10's of centimeters higher than the surrounding strandplain (Fig. 2). Beach ridge 6 has an average elevation of 9.55 ± 0.21 m amsl along a 70 m survey of its crest (Fig. 6). Beach ridge 7 has an average elevation of 11.03 ± 0.17 m amsl along a 170 m survey of its crest. Beach ridge 8 has an average elevation of 11.73 ± 0.20 m amsl along a 120 m survey of its crest. Beach ridge 9 is the fourth stranded beach ridge and is best developed east of the prominent raised tombolo in the study area and south of Cerro Negro (Fig. 2). This is the only location beach ridge 9 is expressed as a prominent stranded beach ridge not partially buried by scree or alluvial fans from more landward platforms or covered by deep snow and ice. A 170 m survey along the crest of beach ridge 9 to the east of a prominent tombolo yielded an average elevation of 13.59 ± 0.19 m amsl (Fig. 6). At this location, beach ridge 9 lies 2.9 m above the seaward strandplain and 2.4 m higher than the landward strandplain between it and the cliffs backing the South Beaches (Fig. 7). What is thought to be the equivalent raised beach ridge to the west of the prominent tombolo is found at a slightly higher elevation and was more difficult to survey given its burial by a snow bank.

4.2. Radar Facies

Six radar facies were identified based on the scheme proposed by Neal (2004) (Fig. 4). The most widespread, the seaward dipping facies (rf-s) consist of moderately continuous, sinuous/wavy and subparallel to oblique/non-parallel, seaward dipping reflections with a true dip (TD) of 6 to 15˚ (Figs. 4, 7, and 8). Landward dipping facies (rf-l) consist of moderately continuous subparallel, parallel/sinuous, landward dipping reflections with a TD of 2-5˚ (Fig. 4). Discontinuous facies (rf-d) consist of discontinuous randomly dipping, semi-chaotic reflections (Fig. 4). Aggradation facies (rf-ag) consist of continuous horizontal and concave-down reflections with low TDs of 1 to 2˚. These facies are often observed draped over seaward topographic breaks in topography (Fig. 4). Flat-lying facies (rf-f) consist of continuous and strong planar horizontal reflections located between beach ridges in topographic lows on the beach surface. Reflections terminate in a planar fashion against bedding with little to no apparent erosion (Fig. 4). Channelized facies (rf-c) consist of chaotic, or lack of reflections overlain by discrete areas where surrounding reflections abruptly terminate and the space between the abrupt terminations is marked by flat lying and continuous reflections that terminate against the same surface.

4.3. Radar Surfaces

Three radar surfaces were identified based on radar reflection terminations (Fig. 5). Radar surface s1-e is defined by reflections onlapping another set of seaward dipping reflections (Fig. 5). This surface most often separates two packages of facies rf-s within the strandplain. Surface s2-b is marked by an increase in hyperbolas overlying ringing multiples and/or regions absent of reflections (Fig. 5). This surface most often separates facies rf-s, and to a lesser extent facies rf-ag and rf-l, above from interpreted bedrock below. Surface s4-tl is marked by toplap of lower seaward dipping reflections below with strong horizontal-planar rf-ag or rf-f reflections above (Fig. 5).

4.4. Beach Architecture

The beach plain was composed of wide strandplains interrupted by 3 to 4 stranded beach ridges on the order of 3 to 5 m's above the surrounding strandplain (Fig. 7 and 8). Additionally, landward of beach ridge 5 was another 2 to 3 weakly developed beaches that lacked the significant relief of the stranded beaches. In general, cobbles and gravels within the strandplain deposits were more angular in nature while the cobbles and gravels within the stranded beach ridge were well rounded and in many cases oblate in shape (Fig. 9). Beach ridge deposits are between 3 and 3.5 m thick while strandplain deposits are between 2 and 2.5 m thick. Thickness varies little within each beach ridge.

Ground penetrating radar profiles across stranded beach ridges 2, 4, and 5 (as well as one example from beach ridge 9) contain facies rf-s separated from the overlying rf-l and rf-ag radar facies by radar surface s1-e (Figs. 7 and 8). A similar architecture is observed within beach ridge 3 as that within the stranded beach ridges: an erosional truncation of radar facies rf-s overlain by facies rf-ag and in some occasions rf-l (Fig. 7). However, beach ridge 3 lacks the bedrock support of a scarp and rests on the seaward flank of stranded beach ridge 4 and 5 deposits, which are underlain by a bedrock scarp (Fig. 8). In stream cuts within beach ridges 2, 4, 5, and 9 immediately along strike of GPR profiles, these seaward steps in elevation of radar surface s2-b appear to correlate with erosional scarps cut into the underlying bedrock platforms draped with beach deposits (Fig. 3). With one potential exception from beach ridge 4, radar facies rf-s is not observed continuously across the bedrock scarps.

The predominant facies observed within the strandplains between these stranded beach ridges is rf-s and to a lesser extent rf-ag (Fig. 7). These facies are separated by seaward dipping erosional surfaces (s1-e) with a TD near that of the rf-s facies. There is one exception landward of beach ridge 9 where rf-s is observed with vertically aggrading bed geometry (Fig. 7c). The flat-lying facies (rf-f) is located overlying the strandplain and seaward dipping reflections (rf-s), which they truncate in some areas (Fig. 7). Facies rf-f are observed with possible interfingering of aggradational facies (rf-ag) in some locations. The channelized facies (rf-c) are located within the strandplain region and appear to erode into both the seaward dipping facies (rf-s) as well as into the top bedrock surface s2-b. Unlike the flat-lying facies (rf-f), no coherent radar facies are located beneath the channelized facies.

4.5. OSL Ages

Forty-six samples were collected for OSL dating. Detailed information on the OSL results can be found in Tables S1 and S2 of the supplementary materials. Although feldspars are generally known to have brighter signals than quartz (e.g. Aitken 1998), only 27 samples had measurable signals (13 cobbles and 14 sediment samples) which were often dim as well. Mineral analysis did identify the grains as plagioclase or potassium feldspars, and further detailed analysis would be necessary to explain the low signal intensities of the samples. The OSL characteristics of the samples were on average poor. Dose recovery tests yielded unreasonably large differences between measured and given doses, well above 10%, and fading rates with g-values larger than 10% per decade made fading corrections impossible. OSL ages ranged in age from 61.7 +/- 11.0 ka to <0.1 ka (Table 1). Samples from the same beach ridge did not always return the same age (Table 1). Only 5 samples could be considered "good.". For those samples, almost all aliquots passed the standard reliability tests and fading rates were low enough to allow fading corrections. For another 4 samples most aliquots passed reliability tests, but their fading rates were high. For those samples we used the ages without fading correction and treated them as minimum ages.

4.6. Sediment Trenches

Sediment trenches provided control to the observations made using GPR. In total, 28 sediment trenches were dug to collect OSL samples. Sedimentary beds of coarse sand between 5 and 15 cm are common within beach ridges. These beds are routinely interrupted by gravel and pebble beds ~5 cm thick. Strandplains contained more silt-sized particles and fewer pebble and cobble beds landward of beach ridge 5. However, beach ridge 8 contains 10 to 15 cm thick sandy gravel beds. Sediment pits from beach ridges 2, 4, 5, and 9 yielded more pebble-rich beds compared to the strandplains. Beach ridge 4, often identified by the coarseness of its surficial deposits, was coarser than the strandplain deposits but notably finer internally than beach ridges 7, 8, and beach 1 (Fig. 9). All pits displayed a pebble veneer at the surface regardless of underlying coarseness. Bedrock was never reached on the Holocene beach ridges within these pits but was observed at depths of 2 to 3 m within stream cuts (Fig. 3).

5. Discussion

5.1. Interpretation of Ground Penetrating Radar

5.1.1. Radar Facies

Radar facies were interpreted based on previous work on sandy and mixed sand and gravel beach ridges (Billy et al., 2014; Carter, 1986; Clemmensen and Nielsen, 2009; Engels and Roberts, 2005; Lindhorst and Schutter, 2014; Souza et al., 2018; Zurbuchen and Simms, 2019). Based on the seaward dip and continuous nature of radar reflections, rf-s is interpreted to be sediments deposited by swash processes on the foreshore during periods of lower wave energy and abundant sediment supply (Fig. 4). The seaward dipping reflections support overall shoreline progradation – likely driven by the overall fall in RSL though the Holocene. Based on the landward dip, radar facies rf-l was interpreted as sediments deposited by overwash processes during periods of increased wave energy or a decrease in sediment supply resulting from strandplain cannibalization and reworking into a beach ridge (McKay and Terich, 1992; Lindhorst and Schutter, 2014) (Fig. 4). The internal complexity to the landward dipping reflections including multiple packages of internal onlapping reflections suggests the overwash likely occurred over an extended period time – likely more than one storm (Fig. 8). Based on its horizontal and concave down orientation and location within topographic highs and upper beds of stranded beach ridges, rf-ag is interpreted as sediments deposited during periods of wave runup and overtopping, which suggests increased wave energy, a decrease in sediment supply, or a rise in RSL (Lindhorst and Schutter, 2014; McKay and Terich, 1992). This aggradational radar facies, rf-ag, is found interfingering with flat lying deposits of rf-f. Erosional truncation is rare within this facies. Based on its chaotic reflections not typically observed in profiles from prograding beaches, radar facies rf-d is interpreted as a region of reworked sediment or a cobble rich bed resting on bedrock attenuating the GPR signal (Fig. 4). Based on its location in topographic lows, horizontal-planar nature, higher silt content within sediment pit LV19-32 along GPR line 25, and observations of lagoons existing between beach ridges, radar facies rf-f is interpreted as lagoon deposits (Fig. 7). Tidal circulation and sedimentation is possible in the lagoons if tidal inlets connected the lagoon with the open ocean when the region between stranded beach ridges was at or below sea level. Tidal inlets were observed on the South Beaches connecting the open ocean with lagoons between beach ridges 2 and 4 and beach 1 and beach ridge 2 (Fig. 3). Fluvial processes are another likely sediment transport mechanism as active streams were observed crosscutting abandoned lagoon deposits to reach the modern lagoon behind beach 1. The armoring of the beach surface observed in every sediment pit suggests fine-grained sediments were winnowed by the wind. Based on observations of fluvial deposits during GPR collection, bedrock erosion and channelization in GPR profiles, landward and seaward dipping reflection orientations, and truncation of older seaward dipping reflections, radar facies rf-c is interpreted as fluvial deposits (Figs. 4 and 7).

5.1.2. Radar Surfaces

Radar surfaces are interpreted following the methods of Lindhorst and Schutter (2014) and Neal (2004) (Fig. 5). Based on the seaward dipping nature of the surfaces and their location between beds of rf-s, radar surface s1-e is interpreted as the result of wave erosion of the strandplain deposits. Lindhorst and Schutter (2014) suggests the degree of shelter a coast receives controls the number of erosional unconformities preserved and therefore the quality of that beach as a recorder of past sea levels. The South Beaches are relatively sheltered due to their south facing direction and contain more erosional surfaces compared to beaches from similar studies in the AP region (Lindhorst and Schutter, 2014; Zurbuchen and Simms, 2019).

Based on the abundance of refraction hyperbolas and/or absence of reflections beneath it, radar surface s2-b is interpreted as the top of the bedrock with a veneer of cobbles (Fig. 5). This bedrock is observed within stream cuts immediately adjacent to beach ridges where bedrock scarps are interpreted in GPR profiles (Fig. 3). Based on its toplap overlain by strong planar horizontal reflections, observations of beach surfaces armored with a pebble veneer, and considering the wind regime of the SSI, radar surface s4-tl is interpreted as an aeolian deflation pavement.

5.2. Beach Ridge Age

We obtained 27 OSL ages from both sand and cobble surfaces. As mentioned above, most of the ages were deemed “unreliable” based on poor OSL characteristics leaving only five of the 27 ages with very good OSL characteristics and another four providing minimum OSL ages. Another potential reason for the poor OSL age agreement is the possibility that the beaches are composite features (e.g. Gardiner et al., 2006). However, in the case of Gardiner et al. (2006) study, the composite nature of the beach ridges was due to their reoccupation over several sea-level highstands at glacial interglacial temporal scales. Only one of our "unreliable" ages predates the LGM, thus the poor age characteristics are not likely a reflection of reoccupation. In addition, outside of the storm-induced surfaces (sl-e) and fluvial facies (rf-f), no other large unconformities within the beach deposits themselves were recognized, which would be expected in the case of reoccupation, suggesting the beach ridges of Livingston Island do not represent composite features at the scale of those identified by Gardiner et al. (2006). Thus, we compared our five "good" ages with 23 radiocarbon ages from the same beach ridges compiled by Hall (2010). In the compilation of Hall (2010), she identified six radiocarbon ages (Table 2) interpreted as dating the formation of the beach with the remaining 17 ages providing only a minimum age of the beach. The formation ages included were from bones incorporated into the framework of the beach deposits at the time of its formation while those samples providing a minimum age of the beach were deposited on top of the beach after its formation (Hall, 2010). We added a 7^{th} unpublished age to those radiocarbon ages, which was obtained from a whalebone sampled from the strandplain between the 1^{st} and 2^{nd} stranded beach ridges at an elevation of 4.7±1.4 m above high tide (determined via barometer) on Cape Sherriff on the northside of Livingston Island ~20 km northeast of the Byers Peninsula (Table 2). This age is interpreted to provide a minimum age of the 1^{st} stranded beach ridge equivalent to our stranded beach ridge 2.

Beach ridge 2 was dated in this study with one reliable OSL cobble age (0.49 ± 0.15 ka or 420 ± 120 cal yrs BP; Table 3; we also note that we had a second "unreliable" OSL age of 0.47 ± 0.12 ka or 400 ± 120 cal yrs BP; Table 1) and by Hall (2010) with three radiocarbon ages: 680 ± 295, 599 ± 289, and 529 ± 289 cal yrs BP (Table 2). These four ages overlap within error. We also interpret our radiocarbon age of 380 ± 292 cal yrs BP (UCIAMS# 270265) to represent a minimum age for this beach ridge. Averaging our OSL age (adjusted to 1950 AD), and three existing radiocarbon ages, suggests an age of 560 ± 525 cal yrs BP for beach ridge 2. Beach ridge 4 was dated in this study with two reliable OSL cobble ages (0.96 ± 0.17 and 2.44 ± 0.39 ka or 890 ± 170 cal yrs BP and 2370 ± 390 cal yrs BP) while closely associated beach ridge 5 is dated by Hall (2010) with three radiocarbon ages: 2206 ± 406, 2199 ± 415, and 1839 ± 390 cal yrs BP. The older of the two OSL ages fits within error of the radiocarbon ages. Thus, we use the average of these four ages (OSL adjusted to 1950 AD) as the age of beach ridges 4 and 5 giving an age of 2155 ± 800 cal yrs BP.

Beach Ridges 7 and 9, which differed in elevation by <2 m were only dated with OSL, but they returned reversed ages with the weakly developed beach ridge 7 at an average elevation of 11.7 m having a sand OSL age of 8.14 ± 1.10 ka (8070 ± 1100 cal yrs BP) and stranded beach ridge 9 at an average elevation of 13.6 m returning an OSL age of 4.19 ± 0.95 ka (4120 ± 950 cal yrs BP). Without radiocarbon ages from these two beaches, it is difficult to determine which age is most likely correct. However, although no ages have been obtained from the highest beach ridge on Livingston Island, radiocarbon ages are available from the higher Holocene beach ridges and marine limit on other islands within the SSI. Nearby on KGI, radiocarbon ages from the highest interpreted Holocene beaches (15.4 to 18.0 m elevation) on Potter and Fildes Peninsulas fall between approximately 5478 ± 637 and 6452 ± 396 cal yrs BP (Sugden and John, 1973; Barsch and Mäusbacher, 1986; Del Valle et al., 2002; Hall, 2010 – recalibrated using the reservoir correction of Divola et al., 2024; Table 2). These KGI beach ages are closer to, and thus might support, the younger OSL age of 4.19 ± 0.95 ka (4120 ± 950 cal yrs BP) obtained for beach ridge 9. However, ages from isolation basins on KGI suggests the marine limit was reached earlier, around 8000 cal yrs BP (Watcham et al., 2011), which would align better with the older OSL age of 8.14 ± 1.10 ka (8070 ± 1100 cal yrs BP) from beach ridge 7. As the ~5900 cal yrs BP ages are derived from raised beach ridges, we favor the OSL age of beach ridge 9 at 4.19 ka (4120 ± 950 cal yrs BP), but acknowledge the large uncertainty in its age.

5.3. Controls on Beach Ridge Architecture

One of the most prominent characteristics of the raised beach plain geomorphology of Byers Peninsula is the prevalence of stranded raised beach ridges 3 to 6 m above the seaward strandplain, separated by 70 to 400 m of lower-lying strandplain. These levels appear to correlate across the SSI (Fretwell et al., 2010). Their formation may reflect a number of potential formative mechanisms including: (1) co-seismic uplift, (2) tsunamis, (3) changes in wave direction and energy, or (4) GIA-induced oscillations in RSL.

5.3.1. Co-seismic uplift (Earthquakes)

One possible mechanism for the formation of the stranded beaches is co-seismic uplift. Coseismic uplift is a common occurrence on some subduction margins. Tectonic uplift of the entire island chain as one block would be needed given the widespread correlation of the raised beaches (Sugden and

John, 1973; Hansom, 1983; Fretwell et al., 2010). Uplift of an area equivalent in size to the whole island chain was observed during the 1964 M9.2 earthquake and tsunami off the coast of Alaska. Uplift of 15 m across an area of 965 km by 210 km were observed (Plafker, 1969) and is more than adequate to encompass the dimensions of the SSI. However, the length of the rupture of the 1964 Alaskan subduction zone earthquake of >800 km (Plafker, 1965) is far greater than the entire SSI trench length of 400 km (Maldonado et al., 1994). Similarly, the paucity of any +5 magnitude earthquakes within the SSI compared to their common occurrence in Alaska (Doser et al., 2002) suggest such large megathrust earthquakes in the SSI are unlikely (Maurice et al., 2003).

The architecture of the stranded beach ridges as recorded in GPR reflections do not fit what might be expected if beach formation were a result of coseismic uplift. Beach material is observed to drape across the seaward edge of scarps that underlie the beach ridges (Figs. 7 and 8). If the beaches were raised predominantly by coseismic uplift, one would not expect to see smaller, less defined “parasitic” beaches (e.g., beach ridge 3) with weaker developed internal beach facies (Fig. 7) on their seaward flanks, which would not exist if coseismic uplift during the Holocene created these beach ridges during a singular event. Furthermore, radar facies rf-s and rf-l truncate across most scarps while rf-ag drapes the scarp. These three separate radar facies are all suggestive of multiple periods of different wave conditions acting during their deposition. Creating three distinct wave conditions during a singular coseismic event would be very unlikely.

Furthermore, the age of stranded raised beaches 2 and 4 is similar to raised beaches with a similar architecture on Joinville Island (Zurbuchen and Simms, 2019; Theilen et al., 2023) (Fig. 10). Joinville Island is not located over the SSI subduction zone and is separated tectonically by spreading within the Bransfield Basin (Maldonado et al., 1994). The similarity in ages within a completely different tectonic setting supports a regional, non-tectonic origin for their development.

5.3.2. Tsunami

Due to the active tectonic setting of the SSI, tsunamis are a likely occurrence on the region’s coastlines. However, a tsunami origin for the stranded beach ridges is unlikely due to their compound sedimentary architecture in that they are composed of several sedimentary packages separated by erosional surfaces (Fig. 8). These surfaces suggest multiple periods of ridge growth separated by erosive surfaces of varying ages. Like coseismic uplift, a tsunami is a one-time event usually creating a single, non-compound feature (Costa and Andrade, 2020). Additionally, tsunamis would impact beaches along different facing coasts with different bathymetric profiles in a non-uniform manner due to their high spatial variability along even a single coastline (Koster et al., 2013). This is not observed in the SSI where beaches in every orientation share similar elevations regardless of orientation towards the Southern Ocean or the Bransfield Basin (Fretwell et al., 2010). The beaches on the northern and southern facing coasts of Byers Peninsula provide a good example of this (Fig. 1).

5.3.3. Wave Energy

Lindhorst and Schutter (2014) proposed a model of gravel beach-ridge plain evolution on nearby KGI to explain the architectural difference between strandplains and beach ridges. Their model of beach formation assumes a constant fall in RSL throughout the Holocene and proposes two modes of beach formation. Mode 1 is net strandplain progradation by swash sedimentation. The progradation and width of the strandplain is controlled by sediment supply and storm interval. Mode 2 is the building of berm ridges due to less sea-ice coverage and increasing storminess, both of which cannibalize the strandplain to build a beach ridge. As beach ridges aggrade vertically, they eventually cross a critical elevation where sediment transport can no longer build the beach ridge (Orford and Carter, 1982; Lindhorst and Schutter, 2014). Following beach ridge abandonment, swash sedimentation and progradation of the strandplain continues stranding the beach ridge. This restarts the model where a new beach ridge forms seaward of the older beach ridge. Lindhorst and Schutter (2014) tested their storm interval and wave energy formation model by comparing three field sites with different wave exposures. They found more beach ridges preserved on more sheltered coasts with fewer but larger beach ridges with more erosional surfaces preserved on more exposed coasts. Additionally, they suggested that an observed change in beach ridge orientations could not be caused by changes in wave action alone but rather was likely influenced by changing basin geometry and ensuing changes in wave refraction as RSL fell. This model may have contributed in some part to the formation of stranded beach ridges, e.g. the landward dipping facies, but this model fails to address the elevation difference between the strandplains landward and seaward of the stranded beach ridges.

5.3.4. Glacial-Isostatic Adjustment (GIA) induced oscillations in RSL

The stranded beach ridges have a few signature characteristics that need to be explained by any model of their formation including their overlying a bedrock scarp and their internal architecture of progradational beach facies overlain by an erosional surface and overwash deposits. Our favored model interpretation for the development of these beach ridges is GIA-induced RSL oscillations (Fig. 11). In our model, facies rf-s, characteristic of strandplain progradation, represents sedimentation during background rates of RSL fall. The erosion to produce the bedrock scarp indicates a slowdown in or cessation of RSL fall or RSL rise accompanied by transgression that eroded into older prograded beach deposits (rf-s) as well as into the underlying bedrock, cutting the scarp observed beneath the stranded beach ridges (Fig. 8). The overlying deposits of rf-l representing overwash may be a reflection of increased water depth with a local RSL rise, allowing larger waves to reach farther inland along the shallow inner parts of the coast. Alternatively, the landward dipping reflections of rf-l could represent a large storm or period of increased storminess. The presence of internal onlap surfaces suggests it is more than a single storm. The landward dipping beds could represent an extended period of more storminess, which we cannot rule out. However, increased storminess alone could not explain the other aspects of the raised beach ridges – their anomalous height and their overlying a bedrock scarp. Then, a return or even an acceleration in RSL fall may have led to the rapid abandonment of the stranded beach ridges (Fig. 11).

What could drive these RSL rises and falls (Fig. 12)? We suggest GIA. Ice advances may lead to local RSL rise causing minor transgressions while their retreat would lead to rejuvenated uplift seen as increased rates of RSL fall (Fig. 11). The homogeneity regardless of shore orientation, varying wave energy, lack of fault scarps, and presence of parasitic beaches on the seaward flank of stranded beach ridges does not align with stranded beach ridge formation by coseismic uplift, higher wave energy, or tsunamis. The granulometry of stranded beach ridge deposits versus strandplain deposits supports our GIA induced model. The strandplain deposits are finer and more angular than those of the stranded beach ridges (Fig. 9). If the stranded beach ridges formed during periods of transgression, the deposits might be expected to be more rounded as they are cannibalized from older beach deposits. Also, if local water depths were deeper, larger waves could transport larger grains. In addition, the glacial advances causing the minor transgressions may have introduced new, larger sediments to the littoral systems (e.g. Hall and Perry, 2004).

Such GIA-driven adjustment of Earth's surface to smaller scale oscillations (as opposed to an LGM-like expansion) in the ice would require a weak rheology similar to what is found beneath the SSI and northern AP (Thomas et al., 2011; Simms et al., 2012; Nield et al., 2014; Simms et al., 2018; Zurbuchen and Simms, 2019). Similarly, these advances likely have a more regional character and thus could explain the similar timing as that seen on Joinville Island (Fig. 10).

5.4. Timing of Scarps and Stranded Beach Ridges: Relationship to Known Ice Advances

One test of our GIA-induced periods of RSL oscillations (Fig. 12) is their timing with respect to known periods of glacial advance and retreat. Previous work has identified evidence of Holocene glacial advances in the SSI and northern AP (Sugden and John, 1973; Curl, 1980; Hall and Perry, 2004; Hall, 2007; Hall, 2009; Hall, 2010; Simms et al., 2012; Guglielmin et al., 2016; Yu et al., 2016, Chu et al., 2017). If the scarps and stranded beach ridges formed due to GIA-induced periods of RSL change, the ages of stranded beach ridges 2, 4 and 5, and 9 should reflect periods of ice retreat after ice advances. The age of stranded beach ridge 2 (560 ± 525 cal yrs BP) is broadly consistent with the end of the Little Ice Age (LIA) (Fig. 12). Local evidence for a LIA at this time includes the work of Hall (2007) who used radiocarbon dating of mosses within moraines on Fildes Peninsula, KGI, to show that the most extensive advance of the Collins Ice Cap within the last ~3500 cal yrs BP occurred after ~650 cal yrs BP. Similarly, Yu et al. (2016) and Guglielmin et al. (2016) both used moss adjacent to ice fronts near Palmer and Rothera stations, respectively, and found evidence of ice advance 760 to 600 cal yrs BP and between 671 to 317 cal yrs BP, respectively. Simms et al. (2021) found evidence of an ice advance on Greenwich Island of the SSI within the last ~375 years. Hall and Perry (2004) used the concentration of IRD on stranded beach ridges 2 and 4 on the South Beaches, Byers Peninsula to infer cooler periods of glacial advance at 250 ^{14}C years BP and 1750 ^{14}C yrs BP, respectively.

Evidence for an ice advance during the time of formation for stranded beach ridges 4 and 5 (2155 ± 800 cal yrs BP) may be found in sediment cores from Domo Lake on Byers Peninsula that were dated using ^{14}C, thermoluminescence, and tephrochronology. Oliva et al. (2016) determined the glacier front readvanced an unknown distance back over Domo Lake after 2300 ± 700 cal yrs BP where it remained until at least 1800 cal yrs BP (Oliva et al., 2016). Similarly, Heredia Barion et al. (2023a, b) found evidence of glacial advance on KGI from 1400 to 1700 cal yrs BP. On nearby James Ross Island, Kaplan et al. (2020) found evidence for a readvance in the form of moraines dated to between ~1000 to 2400 cal yrs BP. Chu et al. (2017) analyzed a 9.24 m sediment core from a fjord on Fildes Peninsula, KGI using ^{14}C, loss on ignition, grain size, magnetic susceptibility, and elements. Within this core, evidence for a neoglacial advance is found between 2700 and 2000 cal yrs BP, at which point the core record ends. Hall and Perry (2004) used the increased IRD concentrations on the beach ridges of Byers Peninsula to suggest an ice advance and cooler conditions during the formation of our beach ridges 4 and 5. Other proxy evidence from the AP supports widespread cooling with glacial advances noted between 2800 and 1400 cal yrs BP (Björck et al., 1996; Domack et al., 2003; Bentley et al., 2009; Michalchuk et al., 2009; Shevenell et al., 2011).

Hall (2009) cites ice advances on the AP and nearby islands that date to ~5500-4500 cal yrs BP and ~8000 to 7000 cal yrs BP based on ^{10}Be CRE dating of glacially polished bedrock. The younger of these correlates with the OSL age of beach ridge 9 while the latter of these at 8000-7000 cal yrs BP is similar to the OSL age of beach ridge 8. However, both beach ridge ages cannot be correct since beach ridge 8 is located seaward of 9. Evidence for advances on the SSI is present for both time periods. Palacios et al. (2020) uses ^{36}Cl and ^{10}Be CRE dating of erratic boulders ~150 m from the Rotch Dome ice front on beach ridges at a reported elevation of 10-12 m on Byers Peninsula, interpreting the ~4000 cal yrs BP age as the timing of a local ice advance. Hansom and Flint (1989) date marine shells of now locally extant species found within glacial till 0.4 m above the high-water mark and under a 10-15 m tall ice cliff on Brabant Island ~200 km SSW of Byers Peninsula. The reservoir-corrected ages suggest they were growing at ~5000 cal yrs BP, which is interpreted to mean ice was at or near its present location before that time. The fresh nature of the shells suggests a neoglacial advance at ~5000 cal yrs BP. In the same core from a fjord on Fildes Peninsula, KGI in which Chu et al. (2017) found evidence of a late neoglacial advance between 2700 and 2000 cal yrs BP, evidence for a period of minor cooling between 5800 and 4800 cal yrs BP was also found. If the beach ridge crest dates the timing of beach ridge abandonment before the last time of marine influence, then our calibrated and isobar correlated age assigned to beach 9 (4120±950 cal yrs BP) falls within the range of known ice advances ~5800-4000 cal yrs BP. The similarity in ages of stranded beach ridges to the timing of known ice advances or cooler periods supports the GIA model response to ice loading (Fig. 12). Preliminary models of GIA suggest small scale Holocene glacial fluctuations are capable of impacting late Holocene RSL of the SSI (Simms et al., 2012), which we observe in the stratigraphic succession of RSL fall and transgression associated facies.

5.5. Implications for the RSL of the SSI

Weak Earth structure within the SSI and the northern AP has previously been attributed to the tectonic and volcanic setting of the region (Taylor et al., 2008; Watcham et al., 2011; Simms et al., 2012; Nield et al., 2014). This weak structure results in heightened sensitivity to surface loading compared to more tectonically stable or cratonic areas. The RSL response to local ice-mass loading suggested in this study supports this notion of sensitivity to Holocene advances. RSL reconstructions in this region assume that the recent uplift reflects GIA from the LGM (Bentley et al., 2005a; Roberts et al., 2011). By documenting significant RSL oscillations driven by Holocene ice fluctuations, our study provides strong empirical support for previous assertions that this recent ice-mass loading generates a GIA signal capable of masking or at the least contaminating the longer-term rebound signal from LGM deglaciation (Simms et al., 2012; Simms et al., 2018; Zurbuchen and Simms, 2019). Therefore, accurately calculating the Antarctic ice mass at the LGM from RSL data requires accounting for these demonstrated Holocene GIA effects.

6. Conclusions

Over 10 km of GPR profiles were collected on the South Beaches of Byers Peninsula, Livingston Island to look for evidence of RSL rise during the overall RSL fall experienced since the LGM. Six radar facies and three radar surface types were identified in the GPR profiles. The radar facies identified included seaward dipping reflections (rf-s) interpreted as prograding beach deposits, landward dipping reflections (rf-l) interpreted as overwash deposits, and a flat and concave-down aggradational facies (rf-ag) interpreted as wave-overtopped deposits. Additional radar facies include a discontinuous reflection configuration interpreted to represent a cobble bed overlying bedrock (rf-d), lagoon facies deposited behind the active beach and connected to the ocean via tidal inlets (rf-f), and fluvial deposits observed on the Holocene beaches and linked to gullies incising the seaward edge of the 28 to 50 m platform (rf-c). Radar surfaces identified include an erosional truncation surface (s1-e), the top of the bedrock, which lacked reflections below and was often covered in cobbles, likely causing ringing hyperbola reflections (s2-b), and a deflation pavement surface (s4-tl) located primarily above rf-s. A repeated succession of facies and surfaces was observed beneath isolated, anomalously high stranded beach ridges. This succession consisted of a seaward scarp in the bedrock overlain by progradational beach deposits (rf-s), in turn overlain by overwash and aggradational beds (rf-l and rf-ag). This succession was observed across scarps beneath stranded beach ridges 9, 4 & 5, and 2. The ages of these beach ridges corresponds to reported glacial advances in the SSI at < 500, ~2000, and ~5000 cal yrs BP.

The succession of surfaces and deposits beneath the stranded beach ridges is interpreted to represent high-frequency oscillations in RSL driven by the GIA response of the earth to local ice advances and retreats during the Holocene. Beaches prograded during RSL fall. Subsequent glacial readvances caused isostatic depression of the earth causing RSL rise and erosion of the shoreline producing the scarps. This RSL rise also increased the local water depth and thus the ability of waves to build and break closer to the shore, resulting in overwash deposition. This process repeats itself during each ice advance that decreases the rate of RSL fall or causes RSL rise, producing the flight of stranded raised beaches observed throughout the SSI.

This study further supports assertions of GIA-induced Holocene transgressions within the SSI during a period of overall RSL fall. The sensitivity to local or regional ice-mass fluctuations recorded in the beach stratigraphy indicates that RSL curves from this region should be applied with caution when used to test GIA predictions of ice-mass loss following the LGM.

Acknowledgements

The authors would like to thank the Captain and crew of the R/V Laurence M. Gould as well as Cara Ferrier and Robin Carroccia for their assistance in access Livingston Island and assisting in the field work, respectively. Marianne Okal helped with the GPS processing. Gareth Seward performed EPMA measurements of feldspar separates. This work was funded through NSF grant 1644197 to ARS and RD and grant 22004488 to ARS. We also thank Chen Ji for his comments on the earthquake potential of the SSI and Claire Divola and John Southon for help in dating the whale bone. We also thank the PALSEA and INSTANT communities for their input presenting these ideas at meetings.

Tables:

sample	Dose (Gy)	g (%/decade)	DR total (Gy/a)	Age unfaded (ka)	Age faded (ka)	Reliable?	Beach Ridge #	Sample Elevation (m)	Comment
LV19-03	6.55 ± 0.25	2.828 ± 0.46	8.16 ± 1.13	0.80 ± 0.11	**0.96 ± 0.17**	*	**4**	7.4	Auclair
LV19-05	5.24 ± 0.2	13.24 ± 0.36	4.25 ± 0.55	**1.23 ± 0.17**			**4**	8.8	**min age**
LV19-07	3.26 ± 0.14	18.99 ± 1.34	5.49 ± 0.56	**0.59 ± 0.07**			**4**	8.9	**min age**
LV19-10	7.94 ± 0.4	13.61 ± 0.59	5.16 ± 0.55	**1.54 ± 0.18**			**9**	13.8	**min age**
LV19-14 (SOSL)	11.09 ± 0.89	7.32 ± 2.3	1.75 ± 0.08	6.34 ± 0.59	**13.05 ± 1.78**		**9**	15.3	Auclair
LV19-16 (SOSL)	7.43 ± 1.33	no fading	2.18 ± 0.09	**3.40 ± 0.62**			**9**	16.5	
LV19-17 (SOSL)	12.14 ± 1.23	no fading	1.25 ± 0.18	**9.68 ± 1.71**			**8**	10.7	
LV19-19	1.23 ± 0.07	9.5 ± 0.73	5.59 ± 0.72	0.22 ± 0.03	**0.47 ± 0.12**		**2**	4.7	Auclair
LV19-21	0.507 ± 0.031	14.22 ± 0.17	0.86 ± 0.09	**0.59 ± 0.07**			**2**	4.5	**min age**
LV19-22	1.075 ± 0.035	9.7 ± 1.3	4.84 ± 0.49	0.22 ± 0.02	**0.49 ± 0.15**	*	**2**	4.6	Auclair
LV19-25 (SOSL)	3.64 ± 0.4	5.6 ± 4.9	1.70 ± 0.16	2.14 ± 0.31	**3.34 ± 3.39**		**2**	4.9	Auclair
LV19-26 (SOSL)	2.94 ± 0.29	4.96 ± 3.2	1.90 ± 0.10	1.55 ± 0.17	**2.23 ± 1.04**		**2**	4.6	Auclair
LV19-27 (SOSL)	5.16 ± 0.71	no fading	1.57 ± 0.06	**3.28 ± 0.47**			**5**	9.5	
LV19-28 (SOSL)	6.06 ± 0.54	no fading	1.64 ± 0.10	**3.70 ± 0.40**			**5**	9.6	
LV19-29	5.41 ± 0.41	no fading	0.65 ± 0.08	**8.35 ± 1.25**			**5**	9.7	
LV19-30 (SOSL)	9.23 ± 0.48	no fading	1.52 ± 0.15	**6.08 ± 0.66**			**4**	8.6	
LV19-31 (SOSL)	5.85 ± 0.26	6.04 ± 5.9	1.63 ± 0.09	3.58 ± 0.26	**5.98 ± 14.09**		**4**	8.6	Auclair
LV19-40 (SOSL)	12.43 ± 0.73	no fading	1.53 ± 0.19	**8.14 ± 1.10**		*	**7**	10.9	
LV19-41 (SOSL)	14.05 ± 1.55	13.6 ± 5.1	1.46 ± 0.19	**9.60 ± 1.61**			**7**	11.1	**min age**
LV19-45	10.18 ± 0.44	7.58 ± 0.39	4.77 ± 0.74	2.13 ± 0.34	**4.19 ± 0.95**	*	**9***	13.9	Auclair
LV19-46	6.87 ± 0.33	no fading	2.42 ± 0.47	**2.84 ± 0.57**			**9***	13.7	
LV19-49 (SOSL)	5.95 ± 0.41	9.06 ± 2	1.27 ± 0.22	4.70 ± 0.88	**12.89 ± 11.62**		**9***	13.7	Auclair
LV19-51 (SOSL)	64.72 ± 4.06 (pre) 80.69 ± 8.32 (post)	3.31 ± 2.2	1.31 ± 0.19		**61.69 ± 10.99**		**7**	10.9	Wallinga
LV19-54 (SOSL)	8.31 ± 1.03	7.7 ± 2	1.46 ± 0.14	5.69 ± 0.90	**12.32 ± 7.17**		**2****	3.9	Auclair
LV19-58	0.151 ± 0.01	8.98 ± 6.73	4.18 ± 0.70	0.04 ± 0.01	**0.05 ± 0.03**		**2**	4.3	Auclair
LV19-59	9.6 ± 0.37	2.835 ± 0.14	4.79 ± 0.68	2.00 ± 0.30	**2.44 ± 0.39**	*	**2**	4.8	Auclair
LV19-60	0.114 ± 0.015	19.1 ± 8.1	4.35 ± 0.68	**0.03 ± 0.01**			1	1.7	**min age**

All samples labelled "LV-x" are rock samples. Samples labelled with "LV-x (SOSL)" are sediment samples.
Dose for LV19-51: The fading correction method by Wallinga et al. (2007) was used. The dose value is given once as measured and once after fading correction.
g-value: fading rate as described by Auclair et al. (2003)
Age unfaded: Dose / Dose rate; no "unfaded" age is quoted for samples where the fading correction method by Wallinga et al. (2007) was used
Age faded: The final age, after fading correction, where applicable.
Beach height: Height of the beach in m, where the sample was collected.
The final age for each sample is in bold print. The fading correction method , either by Auclair et al. (2003) or Wallinga et al. (2007) is cited.
For some samples the fading rate was too high and fading correction was not possible. For those samples a minimum age is given.
Samples that had good luminescence properties and yielded sufficient material are labelled as "reliable".
*On beach east of large tombolo
**Sampled landward of main raised beach ridge 2

Table 1. OSL ages from this study

Lab Code	Material	^{14}C Age	Calendar Age*	Error	ΔR	Reported Sample Elevation (m)	Equivalent Beach Number	Source
SR-1087	Whalebone	3121±35	2206	406	443±135	10.1	5	Hansom, 1979
AA-45934	Bone	3115±47	2199	415	443±135	9	5	Hall, 2010
SR-1086	Whalebone	2823±40	1839	390	443±135	10.3	5	Hansom, 1979
AA-45933	Whalebone	1715±42	680	295	443±135	4	2	Hall, 2010
AA-45932	Whalebone	1625±42	599	289	443±135	5	2	Hall, 2010
AA-45936	Whalebone	1545±46	529	289	443±135	4	2	Hall, 2010
HD9425-910	Pengiuin Bone	6650±90	6452	396	443±135	18	9	Barsch and Mausbacher, 1986
HD8426-910	Pengiuin Bone	6560±55	6355	343	443±135	18	9	Barsch and Mausbacher, 1986
Bed3	Pengiuin Bone	5840±40	5578	339	443±135	15.4	9	Del Valle et al., 2002
Bed5	Pengiuin Bone	5750±40	5478	367	443±135	16.3	9	Del Valle et al., 2002
UCIAMS 270265	Whalebone	1380±50	380	292	443±135	4.7	2**	This study

*Calibrated using Calib 8.2 with the Antarctic marine reservoir of Divola et al. (2024)
**See text

Table 2. Published radiocarbon ages from the raised beaches of Livingston Island used to estimate the ages of the raised beach ridges surveyed in this study.

Beach Number (This Study	Sugden & John (1971) Equivalent SSI Beach	GPS Transect Distance (m)	Elevation m (amsl) ± 2S	Interpreted Age ± 2S (cal yrs BP)
1	modern	800	1.65 ± 0.20	0
2	6m	950	4.29 ± 0.78	560 ± 525
3*	-	*	3.85 ± 0.14	-
4	10m	930	8.06 ± 1.03	2155 ± 800**
5	12m	1410	9.54 ± 0.70	2155 ± 800**
6	-	70	9.55 ± 0.21	-
7	-	170	11.03 ± 0.17	-
8	-	120	11.73 ±0.20	-
9	18m	170	13.59 ± 0.19	4120 ± 950

Table 3. Raised beach ridge numbers, equivalent beaches in literature, elevations, and ages. Dash '-' denotes no corresponding SSI beach. *Beach 3 elevation is computed from a series of individual measurements; the remainder are from calculated GPS transects. **See text.

Figures:

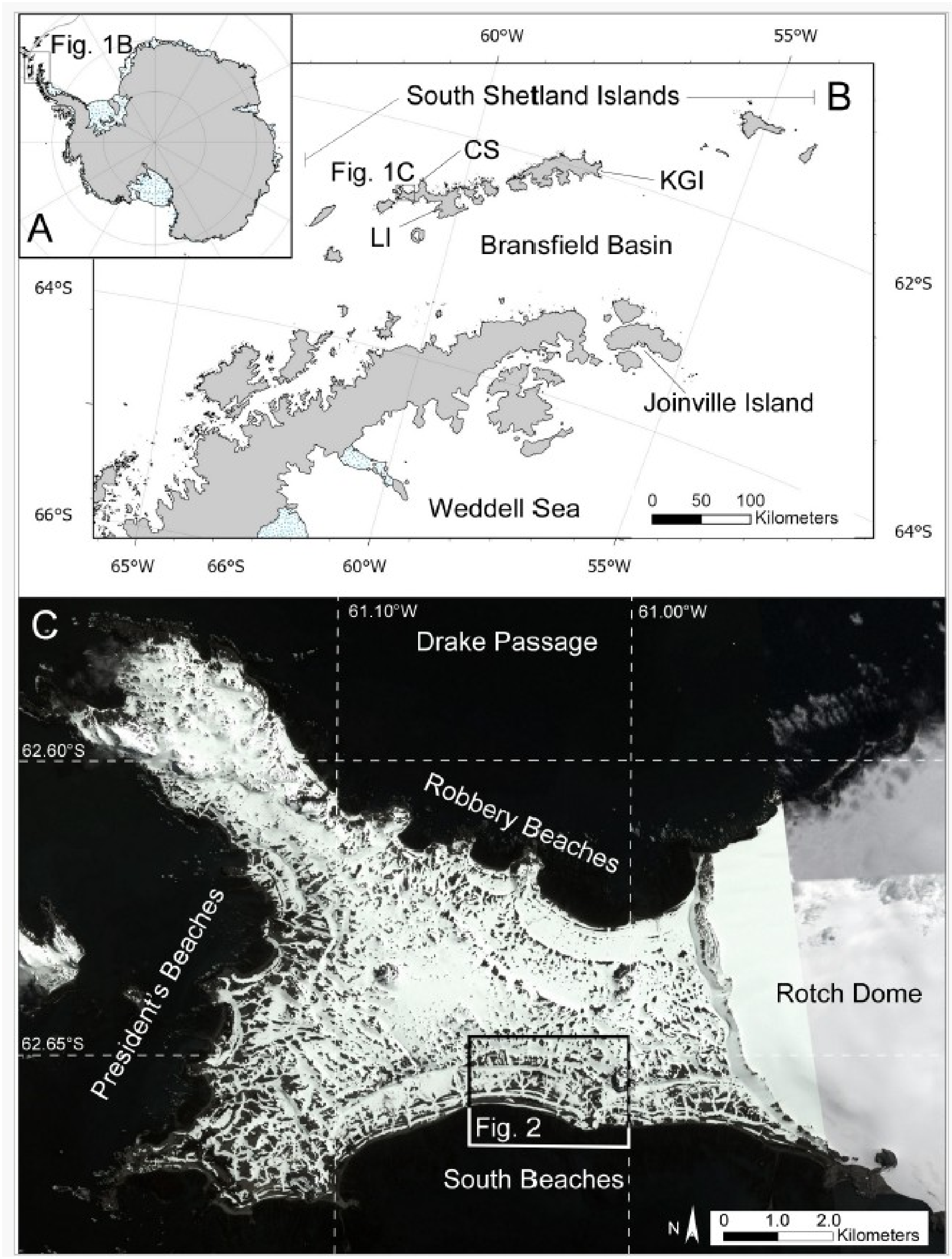

Figure 1. A. Map of Antarctica showing the general location of the northern Antarctica Peninsula and tectonic plate orientation. (B.). C. Satellite photograph (from GoogleEarth) of Byers Peninsula on Livingston Island.

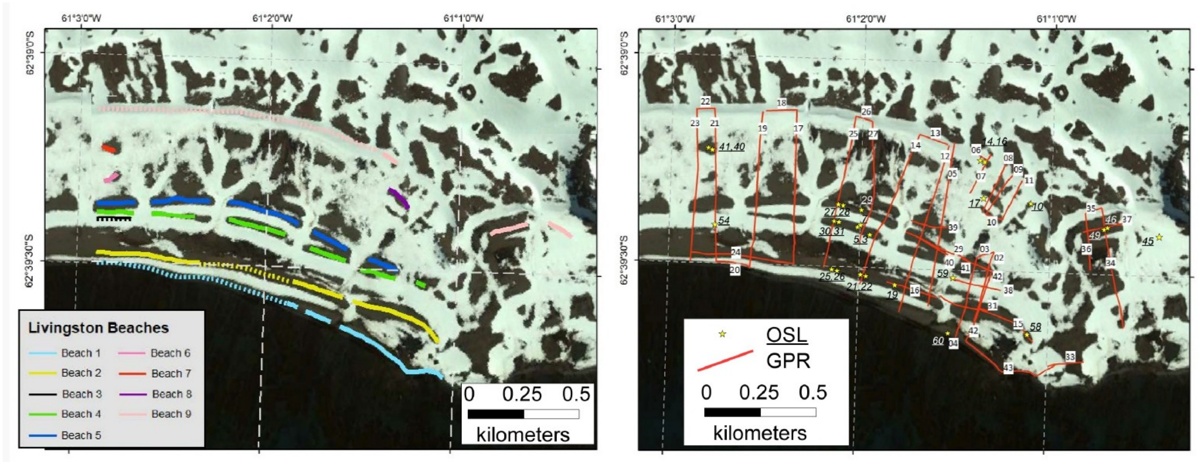

Figure 2. Satellite photograph (from GoogleEarth) of raised beach ridges surveyed in this study (left) and the location of our ground penetrating radar profiles (right).

Figure 3. Photographs of the raised beach ridges and their deposits on the South Beaches of Livingston Island.

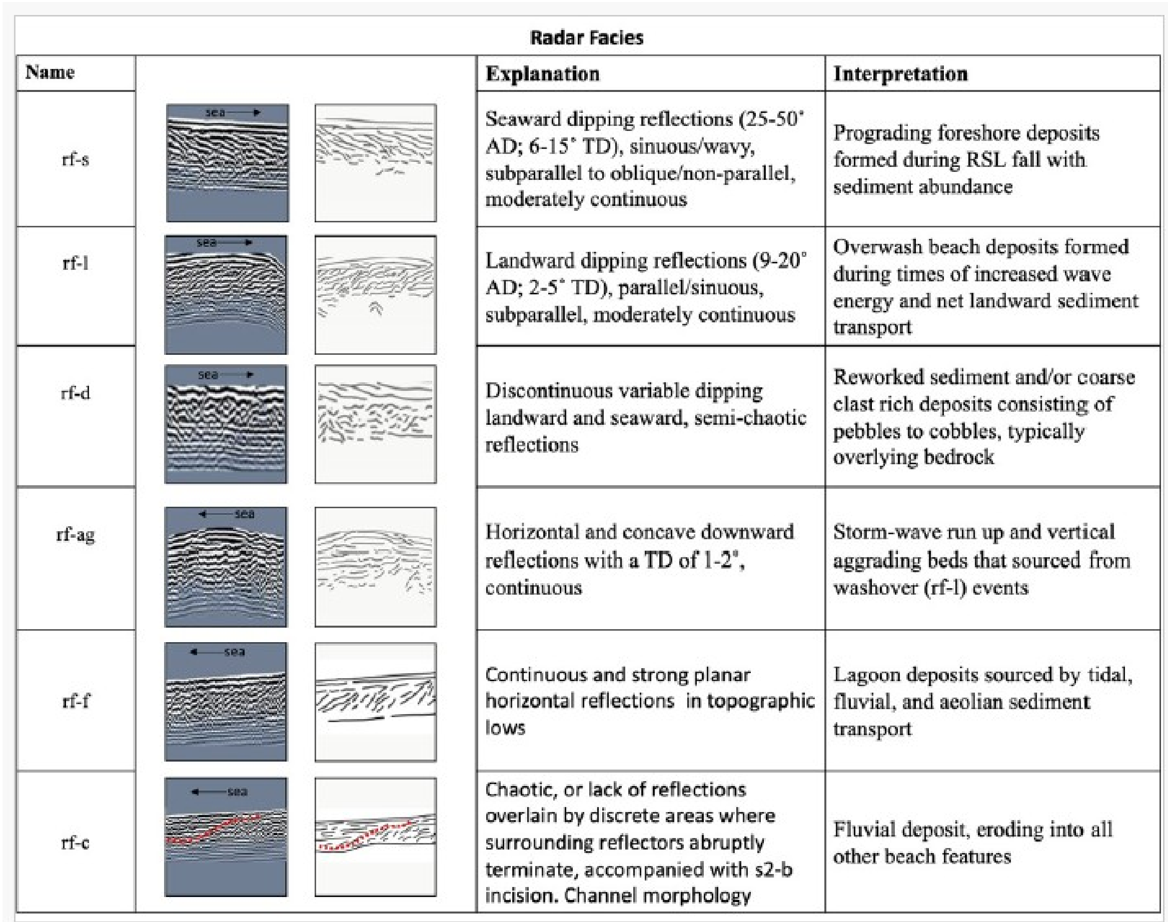

Radar Facies

Name		Explanation	Interpretation
rf-s		Seaward dipping reflections (25-50° AD; 6-15° TD), sinuous/wavy, subparallel to oblique/non-parallel, moderately continuous	Prograding foreshore deposits formed during RSL fall with sediment abundance
rf-l		Landward dipping reflections (9-20° AD; 2-5° TD), parallel/sinuous, subparallel, moderately continuous	Overwash beach deposits formed during times of increased wave energy and net landward sediment transport
rf-d		Discontinuous variable dipping landward and seaward, semi-chaotic reflections	Reworked sediment and/or coarse clast rich deposits consisting of pebbles to cobbles, typically overlying bedrock
rf-ag		Horizontal and concave downward reflections with a TD of 1-2°, continuous	Storm-wave run up and vertical aggrading beds that sourced from washover (rf-l) events
rf-f		Continuous and strong planar horizontal reflections in topographic lows	Lagoon deposits sourced by tidal, fluvial, and aeolian sediment transport
rf-c		Chaotic, or lack of reflections overlain by discrete areas where surrounding reflectors abruptly terminate, accompanied with s2-b incision. Channel morphology	Fluvial deposit, eroding into all other beach features

Figure 4. Summary of the radar facies found within the ground-penetrating radar profiles collected in this study.

Radar Surfaces

Name		Explanation	Interpretation
s1-e	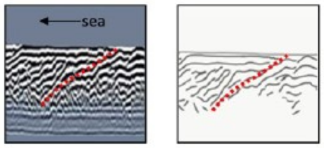	Reflection of terminations in linear arrangement or linear reflection	Erosional surface
s2-b	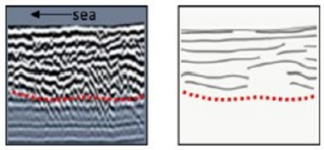	Hyperbola dense layer underlain by ringing multiples and/or absent of reflections	Bedrock covered in cobble pavement
s4-tl	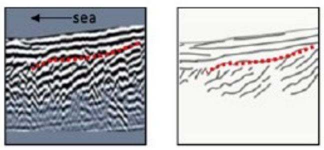	Reflections that pinch out on their upper boundary against the overlying surface or reflector	Deflation surface

Figure 5. Summary of the radar surfaces found within the ground-penetrating radar profiles collected in this study.

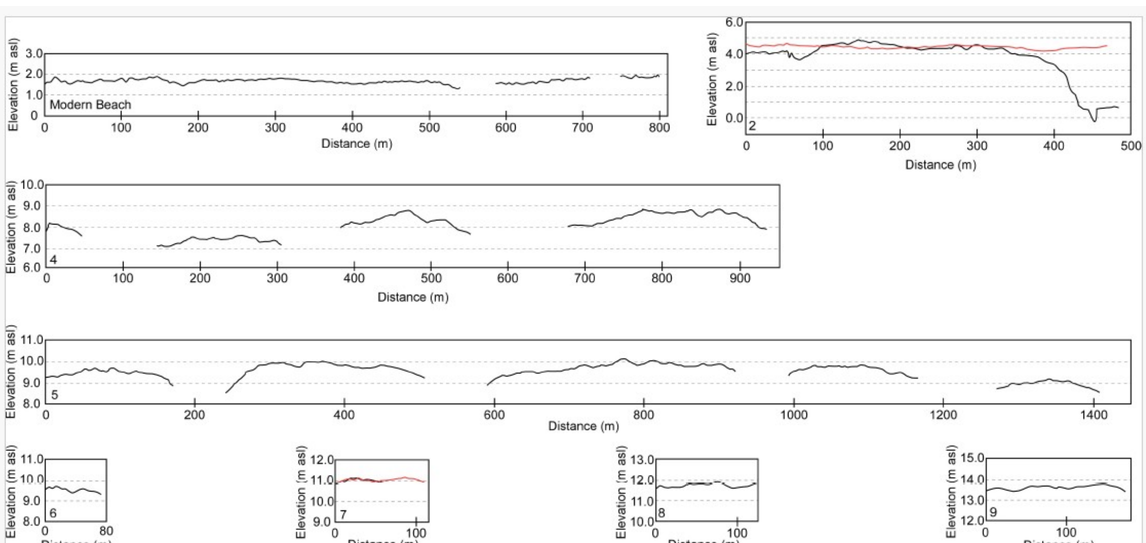

Figure 6. Elevation profiles surveyed along the crests of the modern beach and other raised beach ridges (ridge number in the bottom left hand corner of each profile) on Byers Peninsula.

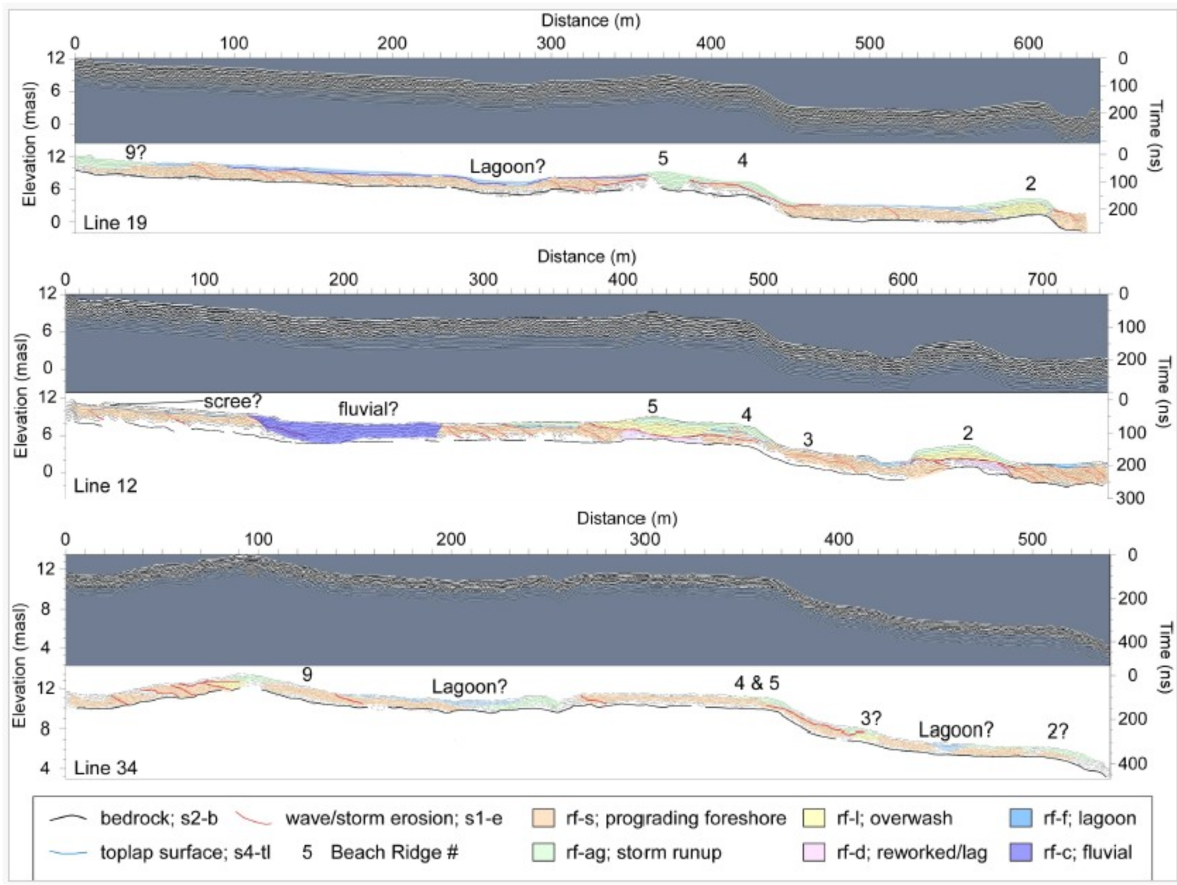

Figure 7. Ground penetrating radar profiles (top) and interpreted reflections and radar facies (bottom) for GPR lines 19, 12, and 34.

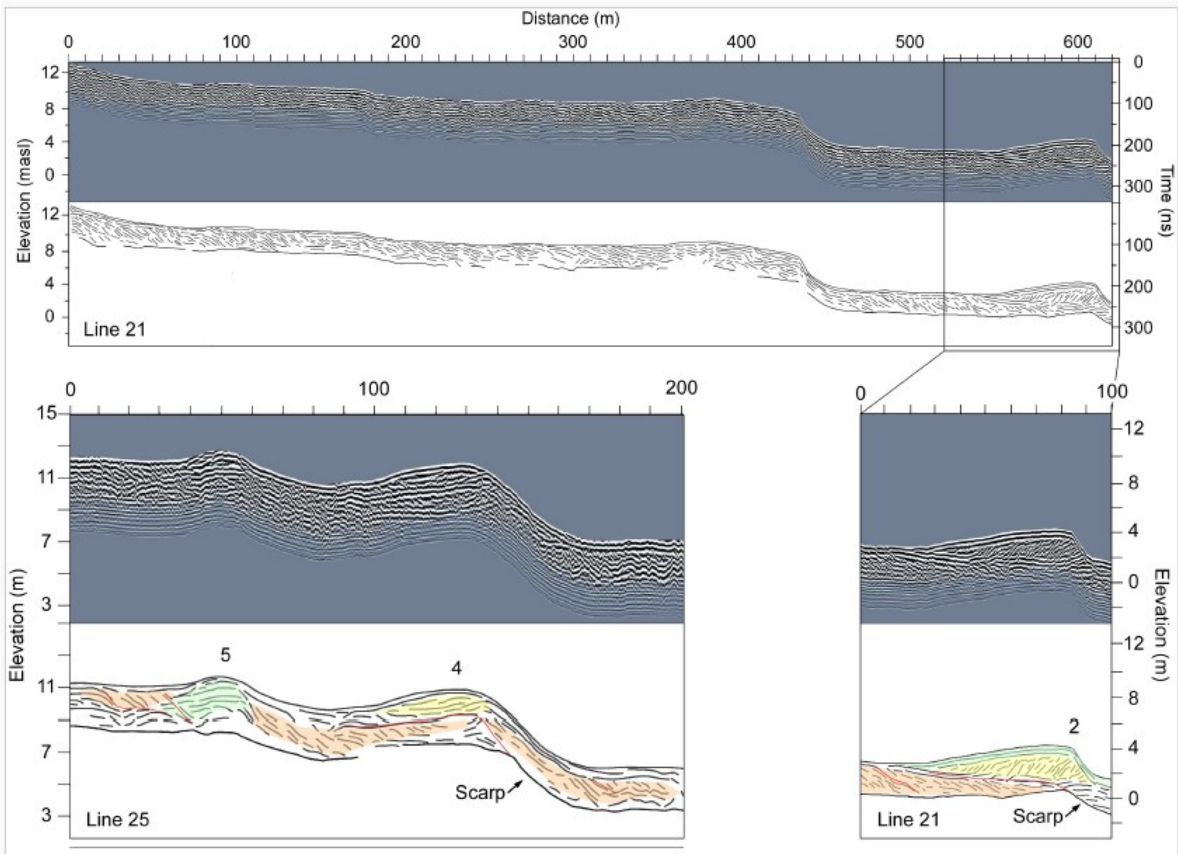

Figure 8. Ground penetrating radar profiles (top) and interpreted reflections and radar facies (bottom) for GPR lines 21 and 25. Inset shows a closer look at the seaward portion of GPR line 21.

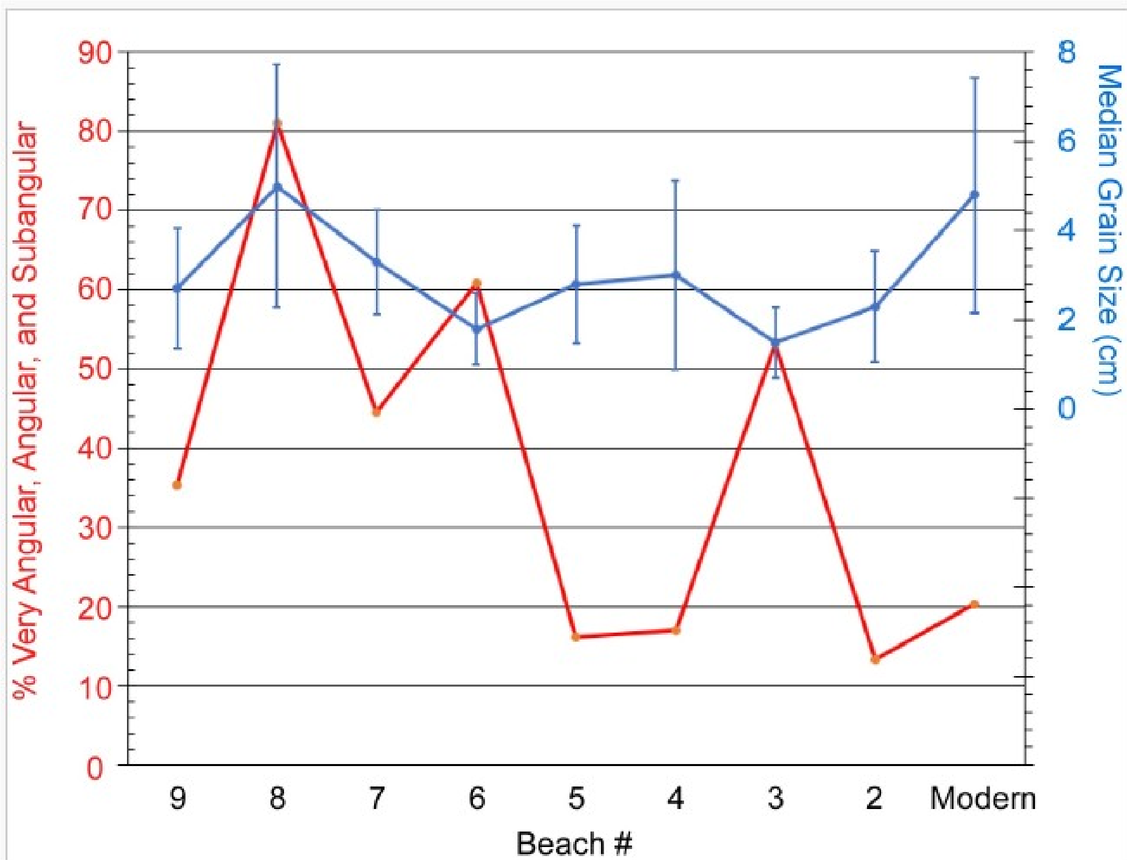

Figure 9. Graph illustrating the angularity (red) and median grain size (blue) for the sediments found on the crests of raised beach ridges 2-9 and the modern beach (beach 1).

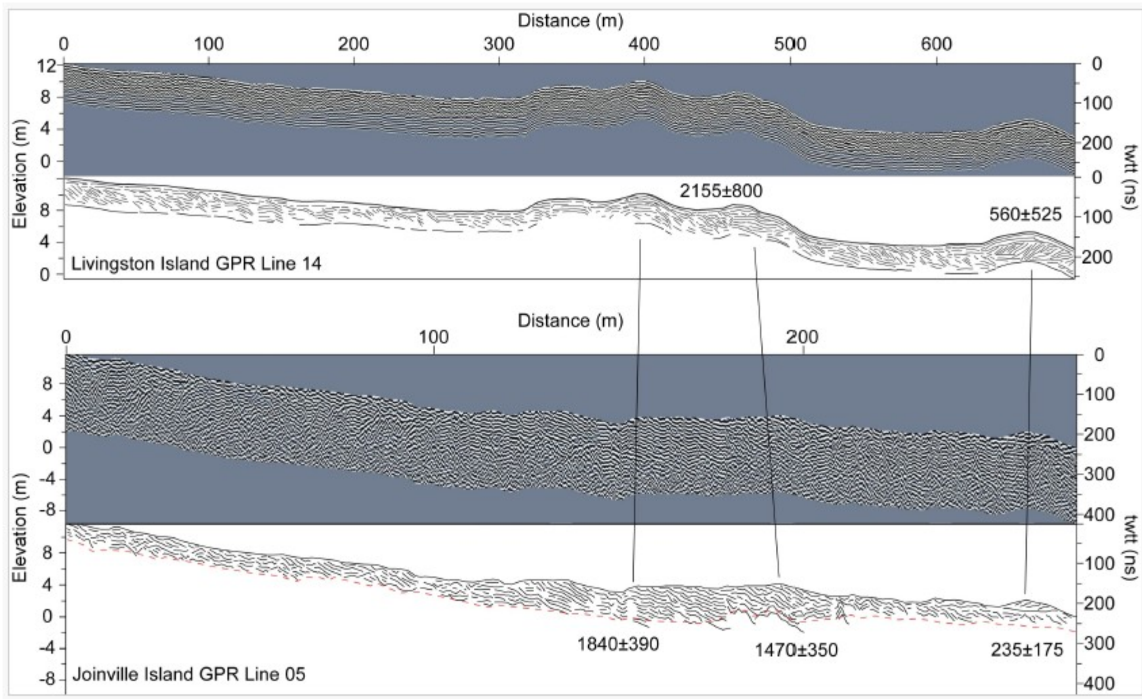

Figure 10. Ground penetrating radar profiles and interpreted reflections on Livingston Island (this study) and Joinville Island (Theilen et al., 2023).

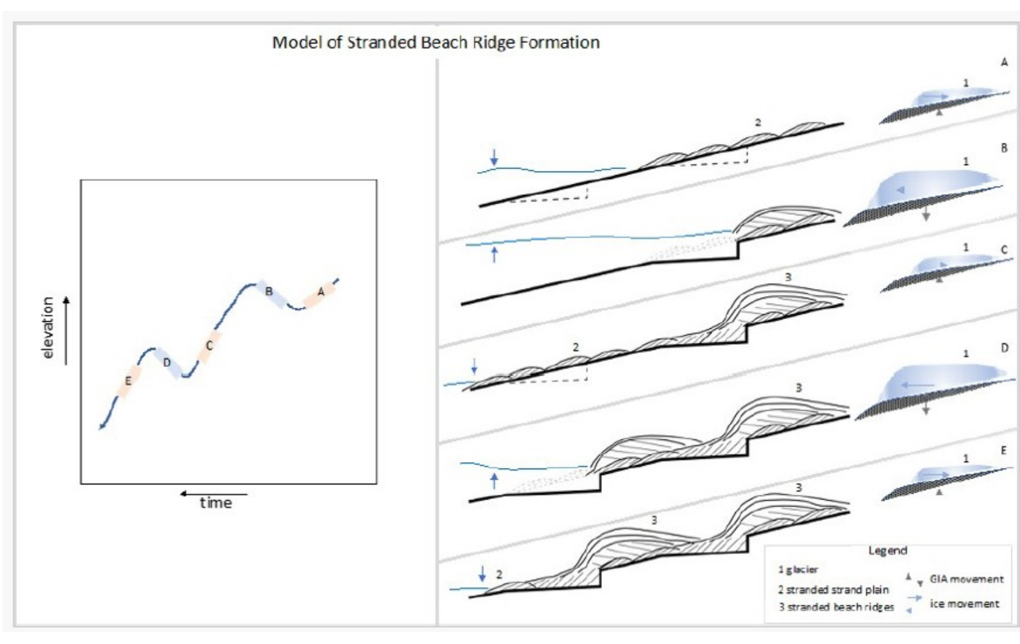

Figure 11. Summary model for the relative sea-level changes (left column), the resulting raised beach ridge stratigraphic architecture (middle), and the expansion and recession of glaciers (right column) on Livingston Island.

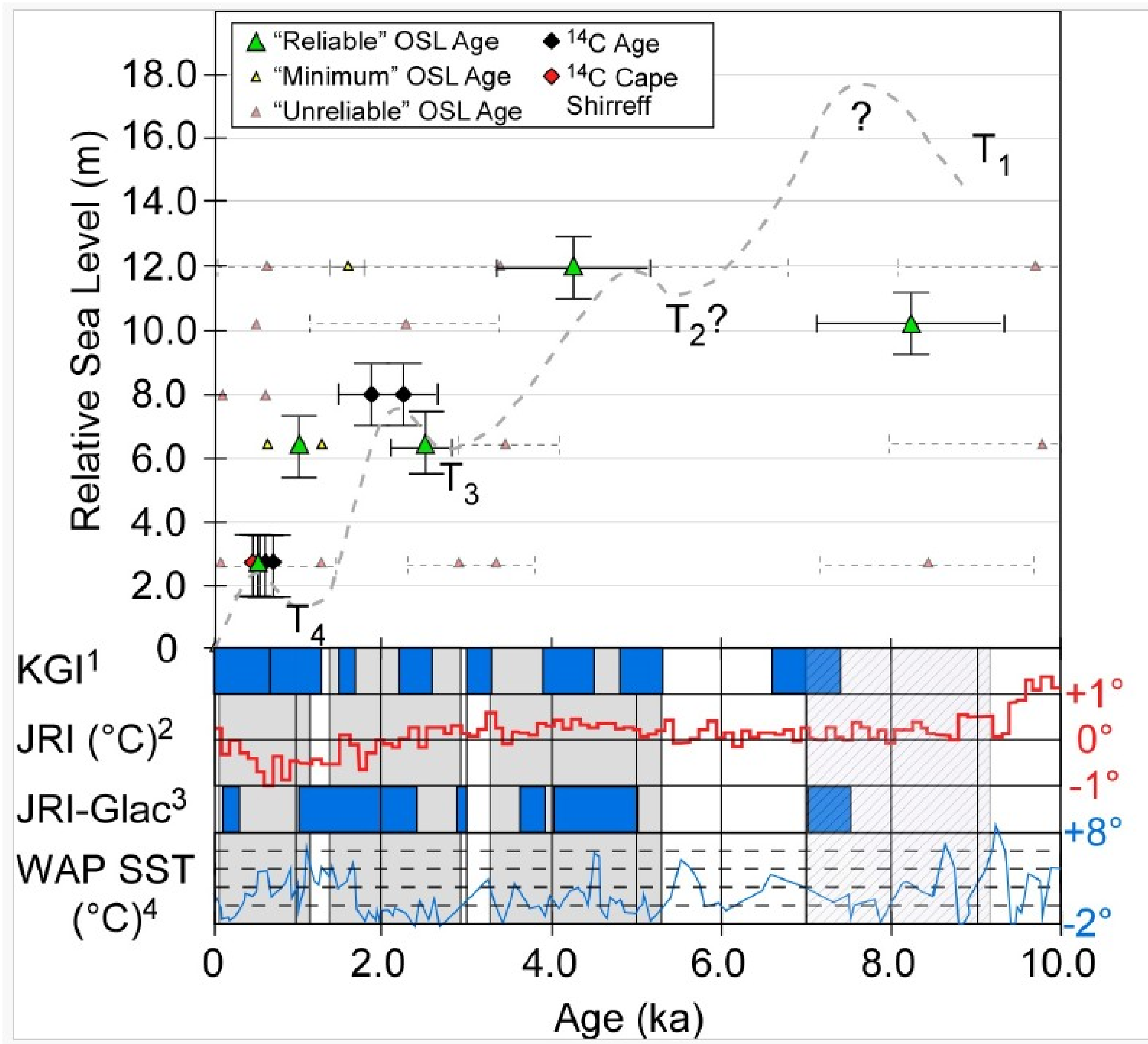

Figure 12. (**Upper**) Interpreted relative sea-level curve for the South Shetland Islands plotted against the age and elevation of the raised beaches on the South Beaches of Livingston Island. In order to correct for the indicative meaning of the beach ridges, RSL elevations were obtained by subtracting the elevation of the modern beach (beach 1) from the elevations of the higher beach ridges (e.g. Fretwell et al., 2010). **(Lower)** Chart comparing climatic proxies from the northern Antarctic Peninsula (rows) with the ages of the stranded raised beaches (grey columns) of Livingston Island. [1]Heredia Barion et al. (2023), [2]Mulvaney et al. (2012), [3]Kaplan et al. (2020), and [4]Shevenell et al. (2011).

Supplemental Information:

sample	rock type	mineral	filter combi	grain size (μm)	n measured	n used	PH (°C)	Dose (Gy)	overdisp (%)	g (%/decade)	tc
LV19-03	Hornblende tonalite	K fsp	blue	63-500	40	34	160	6.55 ± 0.25	7	2.828 ± 0.46	4h
LV19-05	Biotite tonalite	mixed fsp	blue	63-500	29	28	180	5.24 ± 0.2	11	13.24 ± 0.36	3.5h
LV19-07	Biotite hornblende tonalite	K fsp	blue	63-500	21	21	180	3.26 ± 0.14	13	18.99 ± 1.34	4h
LV19-10	Biotite hornblende tonalite	K fsp	blue	63-500	28	28	180	7.94 ± 0.4	0	13.61 ± 0.59	4h
LV19-14 (SOSL)		mixed fsp	blue	90-212	69	32	160	11.09 ± 0.89	25	7.32 ± 2.3	4h
LV19-16 (SOSL)		Na fsp	blue	63-212	57	19	180	7.43 ± 1.33	46	no fading	
LV19-17 (SOSL)		K fsp	blue	63-212	54	21	160	12.14 ± 1.23	23	no fading	
LV19-19	hornblende tonalite	K fsp	blue	63-500	30	20	150	1.23 ± 0.07	20	9.5 ± 0.73	4h
LV19-21	hornblende tonalite	mixed fsp	blue	63-500	36	15	160	0.507 ± 0.031	16	14.22 ± 0.17	3.5h
LV19-22	biotite hornblende tonalite	K fsp	blue	63-500	43	27	160	1.075 ± 0.035	2.7	9.7 ± 1.3	3.5h
LV19-25 (SOSL)		Kfsp	blue	63-212	47	21	160	3.64 ± 0.4	30	5.6 ± 4.9	4h
LV19-26 (SOSL)		Kfsp	blue	63-212	44	17	180	2.94 ± 0.29	32	4.96 ± 3.2	4.5h
LV19-27 (SOSL)		Na fsp	blue	125-150	59	15	160	5.16 ± 0.71	18	no fading	
LV19-28 (SOSL)		K fsp	yellow	150-212	47	21	180	6.06 ± 0.54	16	no fading	
LV19-29	Monzodiorite/diorite (fine-grained)	K fsp	yellow	63-212	72	22	160	5.41 ± 0.41	19	no fading	
LV19-30 (SOSL)		K fsp	blue	63-212	63	36	160	9.23 ± 0.48	9	no fading	
LV19-31 (SOSL)		K fsp	blue	150-212	66	23	180	5.85 ± 0.26	0?	6.04 ± 5.9	3.5h
LV19-40 (SOSL)		K fsp	blue	63-212	52	39	180	12.43 ± 0.73	14	no fading	5h
LV19-41 (SOSL)		K fsp	blue	63-212	79	24	170	14.05 ± 1.55	25	13.6 ± 5.1	4h
LV19-45	hornblende tonalite	K fsp	blue	63-500	34	34	160	10.18 ± 0.44	8	7.58 ± 0.39	4.5h
LV19-46	hornblende tonalite	mixed fsp	blue	63-500	58	36	180	6.87 ± 0.33	20	no fading	3.5h
LV19-49 (SOSL)		K fsp	blue	63-212	53	22	160	5.95 ± 0.41	22	9.06 ± 2	4h
LV19-51 (SOSL)		K fsp	blue	63-212	41	29	170	64.72 ± 4.06 (pre)	24	3.31 ± 2.2	5h
						29		80.69 ± 8.32 (post)	42		
LV19-54 (SOSL)		K fsp	blue	63-212	50	19	180	8.31 ± 1.03	43	7.7 ± 2	4h
LV19-58	hornblende tonalite	mixed fsp	blue	63-500	26	15	160	0.151 ± 0.01	12	8.98 ± 6.73	4h
LV19-59	biotite hornblende tonalite	K fsp	blue	63-500	30	28	180	9.6 ± 0.37	8	2.835 ± 0.14	4h
LV19-60	biotite hornblende tonalite	K fsp	blue	63-500	17	8	150	0.114 ± 0.015	26	19.1 ± 8.1	3.5h

All samples labelled "LV-x" are rock samples. Samples labelled with "LV-x (SOSL)" are sediment samples.
minerals: For samples with sufficient materials, feldspars were separated into K-feldspar (<2.58) and Na-feldspar (>2.58). For all other samples the fraction <2.62 was measured as "mixed" feldspars.
filter combi: in general the brightest signal was used for dating. For most mixed feldspars and K-feldspars this was the blue signal, while Na-feldspars were brighter in yellow. There are some exceptions as listed.
grain size: the grain size obtained after sifting of sediments or after crushing and sifting of rock slizes
n measured and n used: the number of aliquots that were measured for a sample and the number of resulting reliable aliquots that were ued for dose calculation
PH: preheat temperature resulting from plateau and dose recovery tests
overdisp: the overdisperion of the dose values as determined from the central age model (Galbraith, 1999)
g-value: fading rate as described by Auclair et al. (2003)
tc: reference time for fading measurement (Auclair et al, 2003)
LV19-51: The fading correction method by Wallinga et al (2007) was used. The dose value is given once as measured and once after fading correction.

Table S1. OSL Doses

sample	rock type	mineral	filter combi	grain size (μm)	n measured	n used	PH (°C)	Dose (Gy)	overdisp (%)	g (%/decade)	tc
LV19-03	Hornblende tonalite	K fsp	blue	63-500	40	34	160	6.55 ± 0.25	7	2.828 ± 0.46	4h
LV19-05	Biotite tonalite	mixed fsp	blue	63-500	29	28	180	5.24 ± 0.2	11	13.24 ± 0.36	3.5h
LV19-07	Biotite hornblende tonalite	K fsp	blue	63-500	21	21	180	3.26 ± 0.14	13	18.99 ± 1.34	4h
LV19-10	Biotite hornblende tonalite	K fsp	blue	63-500	28	28	180	7.94 ± 0.4	0	13.61 ± 0.59	4h
LV19-14 (SOSL)		mixed fsp	blue	90-212	69	32	160	11.09 ± 0.89	25	7.32 ± 2.3	4h
LV19-16 (SOSL)		Na fsp	blue	63-212	57	19	180	7.43 ± 1.33	46	no fading	
LV19-17 (SOSL)		K fsp	blue	63-212	54	21	160	12.14 ± 1.23	23	no fading	
LV19-19	hornblende tonalite	K fsp	blue	63-500	30	20	150	1.23 ± 0.07	20	9.5 ± 0.73	4h
LV19-21	hornblende tonalite	mixed fsp	blue	63-500	36	15	160	0.507 ± 0.031	16	14.22 ± 0.17	3.5h
LV19-22	biotite hornblende tonalite	K fsp	blue	63-500	43	27	160	1.075 ± 0.035	2.7	9.7 ± 1.3	3.5h
LV19-25 (SOSL)		Kfsp	blue	63-212	47	21	160	3.64 ± 0.4	30	5.6 ± 4.9	4h
LV19-26 (SOSL)		Kfsp	blue	63-212	44	17	180	2.94 ± 0.29	32	4.96 ± 3.2	4.5h
LV19-27 (SOSL)		Na fsp	blue	125-150	59	15	160	5.16 ± 0.71	18	no fading	
LV19-28 (SOSL)		K fsp	yellow	150-212	47	21	180	6.06 ± 0.54	16	no fading	
LV19-29	Monzodiorite/diorite (fine-grained)	K fsp	yellow	63-212	72	22	160	5.41 ± 0.41	19	no fading	
LV19-30 (SOSL)		K fsp	blue	63-212	63	36	160	9.23 ± 0.48	9	no fading	
LV19-31 (SOSL)		K fsp	blue	150-212	66	23	180	5.85 ± 0.26	0?	6.04 ± 5.9	3.5h
LV19-40 (SOSL)		K fsp	blue	63-212	52	39	180	12.43 ± 0.73	14	no fading	5h
LV19-41 (SOSL)		K fsp	blue	63-212	79	24	170	14.05 ± 1.55	25	13.6 ± 5.1	4h
LV19-45	hornblende tonalite	K fsp	blue	63-500	34	34	160	10.18 ± 0.44	8	7.58 ± 0.39	4.5h
LV19-46	hornblende tonalite	mixed fsp	blue	63-500	58	36	180	6.87 ± 0.33	20	no fading	3.5h
LV19-49 (SOSL)		K fsp	blue	63-212	53	22	160	5.95 ± 0.41	22	9.06 ± 2	4h
LV19-51 (SOSL)		K fsp	blue	63-212	41	29	170	64.72 ± 4.06 (pre)	24	3.31 ± 2.2	5h
						29		80.69 ± 8.32 (post)	42		
LV19-54 (SOSL)		K fsp	blue	63-212	50	19	180	8.31 ± 1.03	43	7.7 ± 2	4h
LV19-58	hornblende tonalite	mixed fsp	blue	63-500	26	15	160	0.151 ± 0.01	12	8.98 ± 6.73	4h
LV19-59	biotite hornblende tonalite	K fsp	blue	63-500	30	28	180	9.6 ± 0.37	8	2.835 ± 0.14	4h
LV19-60	biotite hornblende tonalite	K fsp	blue	63-500	17	8	150	0.114 ± 0.015	26	19.1 ± 8.1	3.5h

Table S2. OSL Dose rates

Data Availability

https://www.usap-dc.org/view/dataset/601633

Simms, A. R. (2022) "Ground-Penetrating Radar data from Livingston Island in the Antarctic Peninsula" U.S. Antarctic Program (USAP) Data Center. doi: https://doi.org/10.15784/601633.

References

Adie, R.J., 1964. Stratigraphic correlation in west Antarctica. Antarctic geology, 307, p.313.

Adie, R.J., 1977, Earth sciences: the geology of Antarctica: a review: Philosophical Transactions of the Royal Society of London. B, Biological Sciences, v. 279, no. 963, pp.123-130.

Aitken, M.J., 1998. An introduction to optical dating : the dating of Quaternary sediments by the use of photon-stimulated luminescence. Oxford ; New York : Oxford University Press, 1998.

Auclair, M., Lamothe, M., Huot, S., 2003. Measurement of anomalous fading for feldspar IRSL using SAR. Radiation Measurements, v. 37, no. 4–5, pp. 487–492, doi: https://doi.org/10.1016/S1350-4487(03)00018-0

Bañón, M., Justel, A., Velázquez, D. and Quesada, A., 2013, Regional weather survey on Byers Peninsula, Livingston Island, South Shetland Islands, Antarctica: Antarctic Science, v. 25, no. 2, pp.146-156.

Barbouti, A., Rastin, B., 1983. A study of the absolute intensity of muons at sea level and under various thicknesses of absorber. Journal of Physics G: Nuclear Physics 9, 1577–1595.

Baroni, C., Hall, B.L., 2004. A new Holocene relative sea-level curve for Terra Nova Bay, Victoria Land, Antarctica. Journal of Quaternary Science 19, 377–396.

Barsch, D. and Mäusbacher, R., 1986, New Data on the Relief Development of the South Shetland Islands, Antarctica: Interdisciplinary Science Reviews, v. 11, no. 2, pp. 211-218, doi: 10.1179/isr.1986.11.2.211.

Barton, C.M., 1965, The geology of the South Shetland Islands: III. The stratigraphy of King George Island: British Antarctic Survey, Scientific Reports, no. 44.

Bateman, M.D., Swift, D.A., Piotrowski, J.A., Sanderson, D.C.W., 2012. Investigating the effects of glacial shearing of sediment on luminescence. Quaternary Geochronology 10, 230-236.

Bentley, M., Hodgson, D., Smith, J., and Cox, N., 2005a, Relative sea level curves for the South Shetland Islands and Marguerite Bay, Antarctic Peninsula: Quaternary Science Reviews, v. 24, no. 10-11, p. 1203-1216.

Bentley, M.J., Hodgson, D.A., Smith, J.A., Cofaigh, C.O., Domack, E.W., Larter, R.D., Roberts, S.J., Brachfeld, S., Leventer, A., Hjort, C. and Hillenbrand, C.D., 2009, Mechanisms of Holocene palaeoenvironmental change in the Antarctic Peninsula region: The Holocene, v. 19, no. 1, pp.51-69.

Bentley, M.J., Hodgson, D.A., Smith, J.A., Cox, N.J., 2005b, Relative sea level curves for the South Shetland Islands and Marguerite Bay, Antarctic Peninsula: Quaternary Science Reviews, v. 24, no. 10-11, pp. 1203-1216, doi:10.1016/j.quascirev.2004.10.004.

Billy, J., Robin, N., Hein, C.J., Certain, R., FitzGerald, D.M., 2014, Internal architecture of mixed sand-and-gravel beach ridges: Miquelon-Langlade Barrier, NW Atlantic: Marine Geology, v. 357, p. 53-71, http://dx.doi.org/10.1016/j.margeo.2014.07.011.

Björck, S., Hjort, C., Ingólfsson, O., Zale, R., and Ising, J., 1996, Holocene deglaciation chronology from lake sediments, Geomorphological Map of Byers Peninsula, Livingston Island. Bas Geomap Series Sheet 5-a, British Antarctic Survey, pp. 49-51.

Blair, M.W., Kalchgruber, R., McKeever, S.W.S., 2007. Developing Luminescence Dating for Extraterrestrial Applications: Characterization of Martian Simulants and Minerals. Radiation Measurements 42, p. 392 – 399.

Carter, R.W.G., 1986, The morphodynamics of beach ridge formation: Magilligan, Northern Ireland: Marine Geology, v. 73, p. 191-214.

Charman, D.J., Amesbury, M.J., Roland, T.P., Royles, J., Hodgson, D.A., Convey, P., Griffiths, H., 2018. Spatially coherent late Holocene Antarctic Peninsula surface air temperature variability. Geology 46, 1071–1074.

Chu, Z., Sun, L., Wang, Y., Huang, T. and Zhou, X., 2017, Depositional environment and climate changes during the Holocene in Grande valley, Fildes peninsula, King George Island, Antarctica: Antarctic Science, v. 29, no. 6, pp.545-554.

Clemmensen, L.B., and Nielsen, L., 2009, Internal architecture of a raised beach ridge system (Anholt, Denmark) resolved by ground-penetrating radar investigations: Sedimentary Geology, v. 223, p. 281-290, doi:10.1016/j.sedgeo.2009.11.014.

Costas, S., Ferreira, Ó., Plomaritis, T.A. and Leorri, E., 2016, Coastal barrier stratigraphy for Holocene high-resolution sea-level reconstruction: Scientific reports, v. 6, no. 1, pp.1-12.

Costa, P.J. and Andrade, C., 2020. Tsunami deposits: Present knowledge and future challenges: Sedimentology, v. 67, no. 3, pp.1189-1206.

Curl, J. E., 1980, A glacial history of the South Shetland Islands, Antarctica: Institute of Polar Studies, The Ohio State University.

Del Valle, R.A., Montalti, D. and Inbar, M., 2002. Mid-Holocene macrofossil-bearing raised marine beaches at Potter Peninsula, King George Island, South Shetland Islands. Antarctic Science, v. 14, pp.263-269.

De Pablo, M.A., Ramos, M. and Molina, A., 2014, Thermal characterization of the active layer at the Limnopolar Lake CALM-S site on Byers Peninsula (Livingston Island) : Antarctica: Solid Earth, v. 5, no. 2, pp.721-739.

Divola, C, Simms, A.R., Sremba, A., Baker, C.S., Friedlaender, A., and Southon, J. 2024. Constraining the radiocarbon reservoir age for the Southern Ocean using whale bones salvaged from early 20th century whaling stations. Quaternary Science Reviews, v. 336, p. 108756.

Domack, E.W., Leventer, A., Root, S., Ring, J., Williams, E., Carlson, D., Hirshorn, E., Wright, W., Gilbert, R., Burr, G., 2003. Marine sedimentary record of natural environmental variability and recent warming in the Antarctic Peninsula. Antarctic Research Series 79, 205–224.

Doser, D.I., Brown, W.A., and Velasquez, M., 2002. Seismicity of the Kodiak Island region (1964-2001) and its relation to the 1964 Great Alaskan Earthquake: Bulletin of the Seismological Society of America, v. 92, p. 3269-3292.

Engels, S., and Roberts, M.C., 2005, The architecture of prograding sandy-gravel beach ridges formed during the last Holocene highstand: Southwestern British Columbia, Canada: Journal of Sedimentary Research, v. 75, pp. 1052-1064, doi:10.2110/jsr.2005.081.

Evans, D., Lautenbacher, C., Spinrad, R., and Szabados, M., 2003, Computational techniques for tidal datums handbook: NOAA Special Publication NOS CO-OPS, v. 2.

Fretwell, P.T., Hodgson, D.A., Watcham, E.P., Bentley, M.J., Roberts, S.J., 2010, Holocene isostatic uplift of the South Shetland Islands, Antarctic Peninsula, modelled from raised beaches: Quaternary Science Reviews, v. 29, pp. 1880-1893, doi:10.1016/j.quascirev.2010.04.006.

Galbraith, R.F., Roberts, R.G., Laslet, G.M., Yoshida, H., and Olley, J.M., 1999. Optical dating of single and multiple grains of quartz from Jinmium rock shelter, northern Australia: Part I, Experimental design and statistical models. Archaeometry 41, 339-364.

Gardner, N., Hall, B. and Wehmiller, J., 2006. Pre-Holocene raised beaches at Cape Ross, Southern Victoria Land, Antarctica. Marine Geology, 229(3-4), pp.273-284.

Gràcia, E., Canals, M., Farràn, M.L., Sorribas, J. and Pallàs, R., 1997, Central and eastern Bransfield basins (Antarctica) from high-resolution swath-bathymetry data: Antarctic Science, v. 9, no. 2, pp.168-180.

Guérin, G., Mercier, N., Adamiec, G., 2011. Dose-rate conversion factors: update. Ancient TL 29, 5-8.

Guglielmin, M., Convey, P., Malfasi, F. and Cannone, N., 2016, Glacial fluctuations since the 'Medieval warm period' at Rothera Point (western Antarctic Peninsula): The Holocene, v. 26, no. 1, pp.154-158.

Hall, B.L., 2003, An overview of late Pleistocene glaciation in the South Shetland Islands: Antarctic Research Series, v. 79, pp. 103-113.

Hall, B.L., 2007, Late-Holocene advance of the Collins Ice Cap, King George Island, South Shetland Islands: The Holocene, v. 17, no. 8, pp. 1253-1258.

Hall, B.L., 2009, Holocene glacial history of Antarctica and the sub-Antarctic islands: Quaternary Science Reviews, v. 28, no. 21-22, pp. 2213-2230.

Hall, B., Henderson, G. M., Baroni, C., and Kellogg, T. B., 2010b, Constant Holocene Southern-Ocean 14C reservoir ages and ice-shelf flow rates: Earth and Planetary Science Letters, v. 296, no. 1-2, pp. 115-123.

Hall, B.L. and Denton, G.H., 1999, New relative sea-level curves for the southern Scott Coast, Antarctica: evidence for Holocene deglaciation of the western Ross Sea: Journal of Quaternary Science, v. 14, no. 7, pp.641-650.

Hall, B.L., 2010, Holocene relative sea-level changes and ice fluctuations in the South Shetland Islands: Global and Planetary Change, v. 74, pp. 15-26, doi:10.1016/j.gloplacha.2010.07.007.

Hall, B.L., and Perry, E.R., 2004, Variations in ice rafted detritus on beaches in the South Shetland Islands: a possible climate proxy: Antarctic Science, v. 16, pp. 339-344.

Hansom, J.D., 1979, Radiocarbon dating of a raised beach at 10 m in the South Shetland Islands, Antarctica: Marine Geology, v. 53, pp.211-229.

Hansom, J.D., 1983, Shore-platform development in the South Shetland islands, Antarctica: Marine Geology, v. 53, no. 3, pp.211-229.

Hansom, J.D. and Flint, C., 1989, Short notes Holocene ice fluctuations on Brabant Island, Antarctic Peninsula: Antarctic Science, v. 1, no. 2, pp.165-166.

Heaton, T.J., Köhler, P., Butzin, M., Bard, E., Reimer, R.W., Austin, W.E., Ramsey, C.B., Grootes, P.M., Hughen, K.A., Kromer, B. and Reimer, P.J., 2020, Marine20—the marine radiocarbon age calibration curve (0–55,000 cal BP): Radiocarbon, v. 62, no. 4, pp.779-820.

Heredia Barion, P.B., Roberts, S.J., Spiegel, C., Binnie, S.A., Wacker, L., Davies, J.., Gabriel, I., Jones, V.J., Blockley, S., Pearson, E.J., Foster, L., Davies, S.J., Roland, T.P., Hocking, E.P., Bentley, M.J., Hodgson, D.A., Hayward, C.L., McCulloch, R.D., Strelin, J.A., Kuhn, G., 2023a. Holocene deglaciation and glacier readvances on the Fildes Peninsula and King George Island (Isla 25 de Mayo), South Shetland Islands, NW Antarctic Peninsula. The Holocene 33, 636–658.

Heredia Barion, P.B., Strelin, J.A., Roberts, S.J., Spiegel, C., Wacker, L., Niedermann, S., Bentley, M.J., Pearson, E.J., Czalbowski, N.T.M., Davies, S.J., Schnetger, B., Grosjean, M., Arcusa, S., Perren, B., Hocking, E.P., Kuhn, G., 2023b. The impact of Holocene deglaciation and glacial dynamics on the landscapes and geomorphology of Potter Peninsula, King George Island (Isla 25 Mayo), NW Antarctic Peninsula. Frontiers in Earth Science 10, 1073075.

Hobbs, G., 1968, The geology of the South Shetland Islands: IV. The geology of Livingston Island, British Antarctic Survey. Smellie, J.L., Pankhurst, R., Thomson, M.R.A. and Davies, R.E.S., 1984. The geology of the South Shetland Islands: VI. Stratigraphy, geochemistry and evolution (V. 87) : British Antarctic Survey.

Hong, S., Lee, M.K., Seong, Y.B. et al. 2021, Holocene sea-level history and tectonic implications derived from luminescence dating of raised beaches in Terra Nova Bay, Antarctica: Geosci J 25, 283–298 (2021). https://doi.org/10.1007/s12303-020-0031-x

IPCC, 2019: Technical Summary [H.-O. Pörtner, D.C. Roberts, V. Masson-Delmotte, P. Zhai, E. Poloczanska, K. Mintenbeck, M. Tignor, A. Alegría, M. Nicolai, A. Okem, J. Petzold, B. Rama, N.M. Weyer (eds.)]. In: IPCC Special Report on the Ocean and Cryosphere in a Changing Climate [H.- O. Pörtner, D.C. Roberts, V. Masson-Delmotte, P. Zhai, M. Tignor, E. Poloczanska, K. Mintenbeck, A. Alegría, M. Nicolai, A. Okem, J. Petzold, B. Rama, N.M. Weyer (eds.)]. In press.

Jin, Y., K., Lee, J., Hong, J.K., and Nam, S.H., 2009. Is subduction ongoing in the South Shetland Trench, Antarctic Peninsula?: new constraints from crustal structures of out trench wall. Geosciences Journal, 13, 59-67.

John, B.S. and Sugden, D.E., 1971, Raised Marine Features and Phases of Glaciation in the South Shetland Islands: British Antarctic Survey Bulletin, No. 25, p. 45-111.

Kaplan, M.R., Strelin, J.A., Schaefer, J.M., Peltier, C., Martini, M.A., Flores, E., Winckler, G., Schwartz, R., 2020. Holocene glacier behavior around the northern Antarctic Peninsula and possible causes. Earth and Planetary Science Letters 534, 116077.

Koster, B., Hadler, H., Vött, A. and Reicherter, K., 2013. Application of GPR for visualising spatial distribution and internal structures of tsunami deposits–Case studies from Spain and Greece.: Zeitschrift für Geomorphologie, Supplementary Issues, v. 57, no. 4, pp.29-45.

Lawver, L.A., Sloan, B.J., Barker, D.H., Ghidella, M., Von Herzen, R.P., Keller, R.A., Klinkhammer, G.P. and Chin, C.S., 1996, Distributed, active extension in Bransfield Basin, Antarctic Peninsula: evidence from multibeam bathymetry: GSA Today, v. 6, no. 11, pp.1-6.

Lindhorst, S., and Schutter, I., 2014, Polar gravel beach-ridge systems: Sedimentary architecture, genesis, and implications for climate reconstructions (South Shetland Islands/Western Antarctic Peninsula): Geomorphology, v. 221, p. 187-203, http://dx.doi.org/10.1016/j.geomorph.2014.06.013.

Maldonado, A., Larter, R.D., Aldaya, F., 1994. Forearc tectonic evolution of the South Shetland Margin, Antarctic Peninsula. Tectonics 13, 1345–1370.

Maurice, R., S.D., Wiens, D.A., Shore, P.J., Vera, E. and Dorman, L.M., 2003, Seismicity and tectonics of the South Shetland Islands and Bransfield Strait from a regional broadband seismograph deployment: Journal of Geophysical Research: Solid Earth, v. 108, no. B10.

Mäusbacher, R., Müller, J. and Schmidt, R., 1989, Evolution of postglacial sedimentation in Antarctic lakes (King George Island): Zeitschrift für Geomorphologie, pp.219-234.

McKay, P.J. and Terich, T.A., 1992, Gravel Barrier Morphology: Olympic National Park, Washington State, U.S.A.: Journal of Coastal Research, v. 8, no. 4, p. 813-829, ISSN 0749-0208.

Michalchuk, B. R., Anderson, J. B., Wellner, J. S., Manley, P. L., Majewski, W., and Bohaty, S., 2009, Holocene climate and glacial history of the northeastern Antarctic Peninsula: the marine sedimentary record from a long SHALDRIL core: Quaternary Science Reviews, v. 28, no. 27-28, p. 3049-3065.

Mulvaney, R., Abram, N.J., Hindmarsh, R.C., Arrowsmith, C., Fleet, L., Triest, J., Sime, L.C., Alemany, O. and Foord, S., 2012. Recent Antarctic Peninsula warming relative to Holocene climate and ice-shelf history. Nature, v. 489, no. 7414, pp.141-144.

Murray, A. S., and Wintle, A. G., 2000, Luminescence dating of quartz using an improved single-aliquot regenerative-dose protocol: Radiation measurements, v. 32, no. 1, p. 57-73.

Neal, A., 2004, Ground-penetrating radar and its use in sedimentology: principles, problems, and progress: Earth-Science Reviews, v. 66, p. 261-330.

Nield, G.A., Barletta, V.R., Bordoni, A., King, M.A., Whitehouse, P.L., Clarke, P.J., Domack, E., Scambos, T.A., Berthier, E., 2014, Rapid bedrock uplift in the Antarctic Peninsula explained by viscoelastic response to recent ice unloading: Earth and Planetary Science Letters, v. 397, p. 32-41.

Nielsen, L., and Clemmensen, L.B., 2009, Sea-level markers identified in ground-penetrating radar data collected across modern beach ridge system in a microtidal regime: Terra Nova, v. 21, p. 474-479, doi: 10.1111/j.1365-3121.2009.00904.x.

Nielsen, L., Bendixen, M., Kroon, A., Hede, M.U., Clemmensen, L.B., Weβling, R. and Elberling, B., 2017, Sea-level proxies in Holocene raised beach ridge deposits (Greenland) revealed by ground-penetrating radar: Scientific Reports, v. 7, no. 1, pp.1-8.

O Cofaigh, C., Davies, B.J., Livingstone, S.J., Smith, J.A., Johnson, J.S., Hocking, E.P., Hodgson, D.A., Anderson, J.B., Bentley, M.J., Canals, M., Domack, E.W., Dowdeswell, J.A., Evans, J., Glasser, N.F., Hillenbrand, C.D., Larter, R.D., Roberts, S.J., Simms, A.R., 2014. Reconstruction of ice-sheet changes in the Antarctic Peninsula since the Last Glacial Maximum. Quaternary Science Reviews 100, 87–110.

Oliva, M., Antoniades, D., Giralt, S., Granados, I., Pla-Rabes, S., Toro, M., Liu, E.J., Sanjurjo, J. and Vieira, G., 2016, The Holocene deglaciation of the Byers Peninsula (Livingston Island, Antarctica) based on the dating of lake sedimentary records: Geomorphology, v. 261, pp.89-102.

Orford, J.D. and Carter, R.W.G., 1982, Crestal overtop and washover sedimentation on a fringing sandy gravel barrier coast, Carnsore Point, Southeast Ireland: Journal of Sedimentary Research, v. 52, no. 1, pp.265-278.

Otvos, E.G., 2000, Beach ridges – definitions and significance: Geomorphology, v. 32, p. 83-108.

Palacios, D., Ruiz-Fernández, J., Oliva, M., Andrés, N., Fernández-Fernández, J. M., Schimmelpfennig, I., Leanni, L., González-Díaz, B., and Team, A., 2020, Timing of formation of neoglacial landforms in the South Shetland Islands (Antarctic Peninsula): Regional and global implications: Quaternary Science Reviews, v. 234, p. 106248.

Pallas, R., James, T.S., Sabat, F., Vilaplana, J.M., Grant, D.R.,1997, Holocene uplift in the South Shetland Islands: evaluation of tectonics and glacio-isostasy: The Antarctic Region: Geological Evolution and Processes, p. 861-868.

Plafker, G., 1965. Tectonic deformation associated with the 1964 Alaska earthquake. Science 148, 1675–1687.

Plafker, G., 1969, Tectonics of the March 27, 1964, Alaska earthquake: U.S. Geological Survey Professional Paper 543–I, 74 p., 2 sheets, scales 1:2,000,000 and 1:500,000, https://pubs.usgs.gov/pp/0543i/.

Pörtner, H.O., Roberts, D.C., Adams, H., Adelekan, I., Adler, C., Adrian, R., Aldunce, P., Ali, E., Ara Begum, R., Bednar-Friedl, B. and Bezner Kerr, R., 2022. Technical summary. Climate change, pp.37-118.

Prescott, J.R. and Stephan, L.G., 1982. The contribution of cosmic radiation to the environmental dose for thermoluminescence dating. PACT, 6, 17-25.

Prescott, J.R. and Hutton, J. T., 1994. Cosmic ray contributions to dose rates for luminescence and ESR dating: large depths and long-term time variations. Radiation Measurements 23, 497–500.

Pritchard, H.D., and Vaughan, D.G., 2007, Widespread acceleration of tidewater glaciers on the Antarctic Peninsula: J. Geophys. Res. Earth Surf. v.112, p. 1-10.

Reimer, P.J., Baillie, M.G., Bard, E., Bayliss, A., Beck, J.W., Bertrand, C.J., Blackwell, P.G., Buck, C.E., Burr, G.S., Cutler, K.B. and Damon, P.E., 2004. IntCal04 terrestrial radiocarbon age calibration, 0-26 cal kyr BP. Radiocarbon, 46(3), pp.1029-1058.

Roberts, S., Hodgson, D. A., Sterken, M., Whitehouse, P. L., Verleyen, E., Vyverman, W., Sabbe, K., Balbo, A., Bentley, M. J., and Moreton, S. G., 2011, Geological constraints on glacio-isostatic adjustment models of relative sea-level change during deglaciation of Prince Gustav Channel, Antarctic Peninsula: Quaternary Science Reviews, v. 30, no. 25-26, p. 3603-3617.

Robertson, S.D.M., Wiens, D., Shore, P.J., Vera, E., Dorman, L.M., 2003. Seismicity and tectonics of the South Shetland Islands and Bransfield Strait from a regional broadband seismograph deployment. Journal of Geophysical Research 108, 2461.

Ruiz-Fernández, J. and Oliva, M., 2016, Relative paleoenvironmental adjustments following deglaciation of the Byers Peninsula (Livingston Island, Antarctica): Arctic, Antarctic, and Alpine Research, v. 48, no.2, pp.345-359.

Scheffers, A., Engel, M., Scheffers, S., Squire, P., and Kelletat, D., 2012, Beach ridge systems–archives for Holocene coastal events?: Progress in Physical Geography, v. 36, no. 1, pp. 5-37.

Shevenell, A., Ingalls, A., Domack, E., and Kelly, C., 2011, Holocene Southern Ocean surface temperature variability west of the Antarctic Peninsula: Nature, v. 470, no. 7333, p. 250.

Simkins, L.M., DeWitt, R., Simms, A.R., Briggs, S., Shapiro, R.S., 2016. Investigation of optically stimulated luminescence behavior of quartz from crystalline rock surfaces: A look forward. Quaternary Geochronology 36, 161–173.

Simkins, L.M., Simms, A.R., and DeWitt, R., 2013, Relative sea-level history of Marguerite Bay, Antarctic Peninsula derived from optically stimulated luminescence-dated beach cobbles: Quaternary Science Reviews, v. 77, pp. 141-155.

Simkins, L.M., Simms, A.R. and DeWitt, R., 2015. Assessing the link between coastal morphology, wave energy and sea ice throughout the Holocene from Antarctic raised beaches. Journal of Quaternary Science, 30(4), pp.335-348.

Simms, A.R., 2023. Quaternary relative sea-level changes at high latitudes, in: Encyclopedia of Quaternary Science. Elsevier, pp. 1–15.

Simms, A.R., Bentley, M., Simkins, L., Zurbuchen, J., Reynolds, L., DeWitt, R., Thomas., E.R., 2021, Evidence for a “Little Ice Age” glacial advance within the Antarctic Peninsula – examples from glacially-overrun raised beaches: Quaternary Science Reviews.

Simms, A.R., DeWitt, R., Kouremenos, P., Drewry, A.M., 2011a, A new approach to reconstructing sea levels in Antarctica using optically stimulated luminescence of cobble surfaces: Quaternary Geochronology, v. 6, pp. 50-60, doi:10.1016/j.quageo.2010.06.004.

Simms, A.R., Ishiwa, T., Hodgson, D.A., Tamura, T., DeWitt, R., 2024. Late Pleistocene sea-level constraints across Antarctica. Quaternary Science Reviews 341, 108879.

Simms, A.R., Ivins, E.R., DeWitt, R., Kouremenos, P., Simkins, L.M., 2012, Timing of the most recent Neoglacial advance and retreat in the South Shetland Islands, Antarctic Peninsula: insights from raised beaches and Holocene uplift rates: Quaternary Science Reviews, v. 47, pp. 41-55, doi:10.1016/j.quascirev.2012.05.013.

Simms, A.R., Milliken, K.T., Anderson, J.B. and Wellner, J.S., 2011b, The marine record of deglaciation of the South Shetland Islands, Antarctica since the Last Glacial Maximum: Quaternary Science Reviews, v. 30, no. 13-14, pp.1583-1601.

Simms, A.R., Whitehouse, P.L., Simkins, L.M., Nield, G., DeWitt, R., Bentley, M.J., 2018, Late Holocene relative sea levels near Palmer Station, northern Antarctic Peninsula, strongly controlled by late Holocene ice-mass changes: Quaternary Science Reviews, v. 199, pp. 49-59.

Smellie, J.L., Pankhurst, R.J., Thomson, M.R.A., Davies, R.E.S., 1984, The Geology of the South Shetland Islands: British Antarctic Survey Scientific Reports, v. 87, pp. 1-85.

Souza, P.E., Kroon, A., Nielsen, L., 2018, Beach-ridge architecture constrained by beach topography and ground-penetrating radar, Itilleq (Laksebugt), south-west Disko, Greenland– implications for sea-level reconstructions: Bulletin of the Geological Society of Denmark, v. 66, pp. 167-179, ISSN 2245-7070.

Sugden, D.E., John, B., 1973. The ages of glacier fluctuations in the South Shetland Islands, Antarctica, in: Palaeoecology of Africa, the Surrounding Islands and Antarctica. Balkema, Cape Town, pp. 141–159.

Tamura, T., 2012, Beach ridges and prograded beach deposits as paleoenvironment records: Earth-Science Reviews, v. 114, pp. 279-297, doi:10.1016/j.earscirev.2012.06.004.

Taylor, F.W., Bevis, M.G., Dalziel, I.W., Smalley Jr, R., Frohlich, C., Kendrick, E., Foster, J., Phillips, D. and Gudipati, K., 2008, Kinematics and segmentation of the South Shetland Islands-Bransfield basin system, northern Antarctic Peninsula: Geochemistry, Geophysics, Geosystems, v.9, no. 4.

Taylor, M.J., Stone, G.W., 1996, Beach-ridges: a review: Journal of Coastal Research, v. 12, pp. 612-621.

Theilen, B., 2020, Changes in beach deposit characteristics on Joinville and Livingston Islands, Antarctica. (master's thesis). University of California Santa Barbara, Santa Barbara, California, available from: https://escholarship.org/content/qt6nr7w3c6/qt6nr7w3c6_noSplash_feb362391cfb1b6968dd556cb164d5c4.pdf.

Theilen, B.M., Simms, A.R., DeWitt, R., Zurbuchen, J., Garcia, C., and Gernant, C., 2023. The impact of the Neoglacial and other environmental changes on the raised beaches of Joinville Island, Antarctica. Antarctic Science, v. 35, p. 418-437.

Thomas, I.D., King, M.A., Bentley, M.J., Whitehouse, P.L., Penna, N.T., Williams, S.D., Riva, R.E., Lavallee, D.A., Clarke, P.J., King, E.C. and Hindmarsh, R.C., 2011, Widespread low rates of Antarctic glacial isostatic adjustment revealed by GPS observations: Geophysical Research Letters, v. 38, no. 22.

Toro, M., Granados, I., Pla, S., Giralt, S., Antoniades, D., Galán, L., Cortizas, A.M., Lim, H.S. and Appleby, P.G., 2013, Chronostratigraphy of the sedimentary record of Limnopolar Lake, Byers Peninsula, Livingston Island, Antarctica: Antarctic Science, v. 25, no. 2, pp.198-212.

Wallinga, J., Bos, A.J., Dorenbos, P., Murray, A.S. and Schokker, J., 2007. A test case for anomalous fading correction in IRSL dating. Quaternary Geochronology, 2(1-4), pp.216-221.

Watcham, E.P., Bentley, M.J., Hodgson, D.A., Roberts, S.J., Fretwell, P.T., Lloyd, J.M., Larter, R.D., Whitehouse, P.I., Leng, M.J., Monien, P., Moreton, S.G., 2011, A new Holocene relative sea level curve for the South Shetland Islands, Antarctica: Quaternary Science Reviews, v. 30, pp. 3152-3170, doi:10.1016/j.quascirev.2011.07.021

Whitehouse, P.L., Bentley, M.J., Milne, G.A., King, M.A. and Thomas, I.D., 2012, A new glacial isostatic adjustment model for Antarctica: calibrated and tested using observations of relative sea-level change and present-day uplift rates. Geophysical Journal International, v. 190, no. 3, pp.1464-1482.

Whitehouse, P. L., 2018, Glacial isostatic adjustment modelling: historical perspectives, recent advances, and future directions: Earth surface dynamics., v. 6, no. 2, pp. 401-429.

Wintle, A.G., Murray, A.S., 2006. A review of quartz optically stimulated luminescence characteristics and their relevance in single-aliquot regeneration dating protocols. Radiation Measurements 41, 369-391.

Yıldırım, C., Çiner, A., Sarıkaya, M.A. and Hidy, A., 2024. Cosmogenic surface exposure (10Be) dating of raised beaches in Marguerite Bay, Antarctic Peninsula: Implications for relative sea-level history. Quaternary Science Reviews 344, 108995.

Yu, Z., Beilman, D.W. and Loisel, J., 2016, Transformations of landscape and peat-forming ecosystems in response to late Holocene climate change in the western Antarctic Peninsula: Geophysical Research Letters, v. 43, no. 13, pp.7186-7195.

Zurbuchen, J., and Simms, A. R., 2019, Late Holocene ice-mass changes recorded in a relative sea-level record from Joinville Island, Antarctica: Geology.